

# Calibration of the charge and energy response of the MicroBooNE liquid argon time projection chamber using muons and protons

## MicroBooNE Collaboration

C. Adams<sup>j</sup> M. Alrashed<sup>l</sup> R. An<sup>k</sup> J. Anthony<sup>c</sup> J. Asaadi<sup>cc</sup> A. Ashkenazi<sup>p</sup>  
 S. Balasubramanian<sup>hh</sup> B. Baller<sup>i</sup> C. Barnes<sup>q</sup> G. Barr<sup>t</sup> V. Basque<sup>o</sup> M. Bass<sup>b</sup> F. Bay<sup>dd</sup>  
 S. Berkman<sup>i</sup> A. Bhandari<sup>o</sup> A. Bhat<sup>z</sup> M. Bishai<sup>b</sup> A. Blake<sup>m</sup> T. Bolton<sup>l</sup> L. Camilleri<sup>g</sup> D. Caratelli<sup>i</sup>  
 I. Caro Terrazas<sup>f</sup> R. Carr<sup>p</sup> R. Castillo Fernandez<sup>i</sup> F. Cavanna<sup>i</sup> G. Cerati<sup>i</sup> Y. Chen<sup>a</sup> E. Church<sup>u</sup>  
 D. Cianci<sup>g</sup> E. O. Cohen<sup>aa</sup> J. M. Conrad<sup>p</sup> M. Convery<sup>x</sup> L. Cooper-Troendle<sup>hh</sup>  
 J. I. Crespo-Anadón<sup>g</sup> M. Del Tutto<sup>t</sup> D. Devitt<sup>m</sup> A. Diaz<sup>p</sup> L. Domine<sup>x</sup> K. Duffy<sup>i</sup> S. Dytman<sup>v</sup>  
 B. Eberly<sup>h</sup> A. Ereditato<sup>a</sup> L. Escudero Sanchez<sup>c</sup> J. Esquivel<sup>z</sup> J. J. Evans<sup>o</sup> R. S. Fitzpatrick<sup>q</sup>  
 B. T. Fleming<sup>hh</sup> N. Foppiani<sup>j</sup> D. Franco<sup>hh</sup> A. P. Furmanski<sup>o</sup> D. Garcia-Gamez<sup>o</sup> S. Gardiner<sup>i</sup>  
 V. Genty<sup>g</sup> D. Goeldi<sup>a</sup> S. Gollapinni<sup>bb</sup> O. Goodwin<sup>o</sup> E. Gramellini<sup>i</sup> P. Green<sup>o</sup> H. Greenlee<sup>i</sup>  
 R. Grosso<sup>e</sup> L. Gu<sup>ff</sup> W. Gu<sup>b</sup> R. Guenette<sup>j</sup> P. Guzowski<sup>o</sup> P. Hamilton<sup>z</sup> O. Hen<sup>p</sup> C. Hill<sup>o</sup>  
 G. A. Horton-Smith<sup>l</sup> A. Hourlier<sup>p</sup> E.-C. Huang<sup>n</sup> R. Itay<sup>x</sup> C. James<sup>i</sup> J. Jan de Vries<sup>c</sup> X. Ji<sup>b</sup>  
 L. Jiang<sup>v</sup> J. H. Jo<sup>hh</sup> R. A. Johnson<sup>e</sup> J. Joshi<sup>b</sup> Y.-J. Jwa<sup>g</sup> G. Karagiorgi<sup>g</sup> W. Ketchum<sup>i</sup>  
 B. Kirby<sup>b</sup> M. Kirby<sup>i</sup> T. Kobilarcik<sup>i</sup> I. Kreslo<sup>a</sup> I. Lepetic<sup>k</sup> Y. Li<sup>b</sup> A. Lister<sup>m</sup> B. R. Littlejohn<sup>k</sup>  
 S. Lockwitz<sup>i</sup> D. Lorca<sup>a</sup> W. C. Louis<sup>n</sup> M. Luethi<sup>a</sup> B. Lundberg<sup>i</sup> X. Luo<sup>hh</sup> A. Marchionni<sup>i</sup>  
 S. Marocci<sup>i</sup> C. Mariani<sup>ff</sup> J. Marshall<sup>gg</sup> J. Martin-Albo<sup>j</sup> D. A. Martinez Caicedo<sup>y</sup> K. Mason<sup>ee</sup>  
 A. Mastbaum<sup>d</sup> N. McConkey<sup>o</sup> V. Meddage<sup>l</sup> T. Mettler<sup>a</sup> K. Miller<sup>d</sup> J. Mills<sup>ee</sup> K. Mistry<sup>o</sup>  
 A. Mogan<sup>bb</sup> T. Mohayai<sup>i</sup> J. Moon<sup>p</sup> M. Mooney<sup>f</sup> C. D. Moore<sup>i</sup> J. Mousseau<sup>q</sup> M. Murphy<sup>ff</sup>  
 R. Murrells<sup>o</sup> D. Naples<sup>v</sup> R. K. Neely<sup>l</sup> P. Nienaber<sup>w</sup> J. Nowak<sup>m</sup> O. Palamara<sup>i</sup> V. Pandey<sup>ff</sup>  
 V. Paolone<sup>v</sup> A. Papadopoulou<sup>p</sup> V. Papavassiliou<sup>r</sup> S. F. Pate<sup>r</sup> A. Paudel<sup>l</sup> Z. Pavlovic<sup>i</sup>  
 E. Piasetzky<sup>aa</sup> D. Porzio<sup>o</sup> S. Prince<sup>j</sup> G. Pulliam<sup>z</sup> X. Qian<sup>b</sup> J. L. Raaf<sup>i</sup> A. Rafique<sup>l</sup> L. Ren<sup>r</sup>  
 L. Rochester<sup>x</sup> H.E. Rogers<sup>f</sup> M. Ross-Lonergan<sup>g</sup> C. Rudolf von Rohr<sup>a</sup> B. Russell<sup>hh</sup>  
 G. Scanavini<sup>hh</sup> D. W. Schmitz<sup>d</sup> A. Schukraft<sup>i</sup> W. Seligman<sup>g</sup> M. H. Shaevitz<sup>g</sup> R. Sharankova<sup>ee</sup>  
 J. Sinclair<sup>a</sup> A. Smith<sup>c</sup> E. L. Snider<sup>i</sup> M. Soderberg<sup>z</sup> S. Söldner-Rembold<sup>o</sup> S. R. Soleti<sup>t,j</sup>  
 P. Spentzouris<sup>i</sup> J. Spitz<sup>q</sup> M. Stancari<sup>i</sup> J. St. John<sup>i</sup> T. Strauss<sup>i</sup> K. Sutton<sup>g</sup> S. Sword-Fehlberg<sup>r</sup>  
 A. M. Szelc<sup>o</sup> N. Tagg<sup>s</sup> W. Tang<sup>bb</sup> K. Terao<sup>x</sup> R. T. Thornton<sup>n</sup> M. Touns<sup>i</sup> Y.-T. Tsai<sup>x</sup> S. Tufanli<sup>hh</sup>  
 T. Usher<sup>x</sup> W. Van De Pontseele<sup>t,j</sup> R. G. Van de Water<sup>n</sup> B. Viren<sup>b</sup> M. Weber<sup>a</sup> H. Wei<sup>b</sup>  
 D. A. Wickremasinghe<sup>v</sup> Z. Williams<sup>cc</sup> S. Wolbers<sup>i</sup> T. Wongjirad<sup>ee</sup> K. Woodruff<sup>r</sup> M. Wospakrik<sup>i</sup>  
 W. Wu<sup>i</sup> T. Yang<sup>i</sup> G. Yarbrough<sup>bb</sup> L. E. Yates<sup>p</sup> G. P. Zeller<sup>i</sup> J. Zennaro<sup>i</sup> C. Zhang<sup>b</sup>

<sup>a</sup>Universität Bern, Bern CH-3012, Switzerland

<sup>b</sup>Brookhaven National Laboratory (BNL), Upton, NY, 11973, USA

<sup>c</sup> *University of Cambridge, Cambridge CB3 0HE, United Kingdom*  
<sup>d</sup> *University of Chicago, Chicago, IL, 60637, USA*  
<sup>e</sup> *University of Cincinnati, Cincinnati, OH, 45221, USA*  
<sup>f</sup> *Colorado State University, Fort Collins, CO, 80523, USA*  
<sup>g</sup> *Columbia University, New York, NY, 10027, USA*  
<sup>h</sup> *Davidson College, Davidson, NC, 28035, USA*  
<sup>i</sup> *Fermi National Accelerator Laboratory (FNAL), Batavia, IL 60510, USA*  
<sup>j</sup> *Harvard University, Cambridge, MA 02138, USA*  
<sup>k</sup> *Illinois Institute of Technology (IIT), Chicago, IL 60616, USA*  
<sup>l</sup> *Kansas State University (KSU), Manhattan, KS, 66506, USA*  
<sup>m</sup> *Lancaster University, Lancaster LA1 4YW, United Kingdom*  
<sup>n</sup> *Los Alamos National Laboratory (LANL), Los Alamos, NM, 87545, USA*  
<sup>o</sup> *The University of Manchester, Manchester M13 9PL, United Kingdom*  
<sup>p</sup> *Massachusetts Institute of Technology (MIT), Cambridge, MA, 02139, USA*  
<sup>q</sup> *University of Michigan, Ann Arbor, MI, 48109, USA*  
<sup>r</sup> *New Mexico State University (NMSU), Las Cruces, NM, 88003, USA*  
<sup>s</sup> *Otterbein University, Westerville, OH, 43081, USA*  
<sup>t</sup> *University of Oxford, Oxford OX1 3RH, United Kingdom*  
<sup>u</sup> *Pacific Northwest National Laboratory (PNNL), Richland, WA, 99352, USA*  
<sup>v</sup> *University of Pittsburgh, Pittsburgh, PA, 15260, USA*  
<sup>w</sup> *Saint Mary's University of Minnesota, Winona, MN, 55987, USA*  
<sup>x</sup> *SLAC National Accelerator Laboratory, Menlo Park, CA, 94025, USA*  
<sup>y</sup> *South Dakota School of Mines and Technology (SDSMT), Rapid City, SD, 57701, USA*  
<sup>z</sup> *Syracuse University, Syracuse, NY, 13244, USA*  
<sup>aa</sup> *Tel Aviv University, Tel Aviv, Israel, 69978*  
<sup>bb</sup> *University of Tennessee, Knoxville, TN, 37996, USA*  
<sup>cc</sup> *University of Texas, Arlington, TX, 76019, USA*  
<sup>dd</sup> *TUBITAK Space Technologies Research Institute, METU Campus, TR-06800, Ankara, Turkey*  
<sup>ee</sup> *Tufts University, Medford, MA, 02155, USA*  
<sup>ff</sup> *Center for Neutrino Physics, Virginia Tech, Blacksburg, VA, 24061, USA*  
<sup>gg</sup> *University of Warwick, Coventry CV4 7AL, United Kingdom*  
<sup>hh</sup> *Wright Laboratory, Department of Physics, Yale University, New Haven, CT, 06520, USA*

E-mail: [microboone\\_info@fnal.gov](mailto:microboone_info@fnal.gov)

**ABSTRACT:** We describe a method used to calibrate the position- and time-dependent response of the MicroBooNE liquid argon time projection chamber anode wires to ionization particle energy loss. The method makes use of crossing cosmic-ray muons to partially correct anode wire signals for multiple effects as a function of time and position, including misconfigured or cross-connected TPC wires, space charge effects, electron attenuation, diffusion, and recombination. The overall energy scale is then determined using fully-contained beam-induced muons originating and stopping in the active region of the detector. Using this method, we obtain an absolute energy scale uncertainty of 3% in data. We use stopping protons to further refine the relation between the measured charge and the energy loss for highly-ionizing particles. This data-driven detector calibration improves both the measurement of total deposited energy and particle identification based on energy loss per unit length as a function of residual range.

---

## Contents

<b>1</b>	<b>Introduction</b>	<b>2</b>
<b>2</b>	<b>dQ/dx Calibration</b>	<b>3</b>
2.1	Introduction	3
2.1.1	Misconfigured or cross-connected TPC channels	3
2.1.2	Space charge effects (SCE)	3
2.1.3	Electron attenuation	5
2.1.4	Diffusion	6
2.1.5	Temporal variations	6
2.1.6	dQ/dx variation	6
2.2	Event selection	7
2.3	Data sample	8
2.4	Analysis method	8
2.4.1	Procedure for detector calibration in the yz plane	9
2.4.2	Procedure for detector calibration in the drift direction	10
2.4.3	Procedure for time dependent calibration of the detector	11
2.5	Results	13
2.5.1	dQ/dx calibration (Simulation)	13
2.5.2	dQ/dx calibration (data)	13
2.6	Angular dependence study	15
<b>3</b>	<b>dE/dx Calibration</b>	<b>16</b>
3.1	Introduction	16
3.2	Event selection	17
3.3	Data sample	18
3.4	Analysis method	18
3.5	Results	19
<b>4</b>	<b>Energy correction with protons</b>	<b>22</b>
4.1	Introduction	22
4.2	Event selection	23
4.3	Analysis method	25
4.3.1	Validation after applying new parameters	27
4.4	Results	27
<b>5</b>	<b>Conclusions</b>	<b>29</b>

---

# 1 Introduction

Liquid argon time projection chamber (LArTPC) technology provides both particle track and energy reconstruction with high resolution. The basic working principle of a LArTPC neutrino detector is that neutrinos first interact with an argon nucleus and produce charged and neutral secondary particles. The charged secondary particles travel through liquid argon and mainly lose their energy by ionizing and exciting argon atoms. The ionization electrons travel under an applied electric field to a set of anode wire planes. The charge is measured on the anode wire planes in order to reconstruct particle trajectories and energies. Excited argon atoms also produce scintillation light, which is detected by the photon detectors. In this paper, we address the calibration of the charge collected at the anode wires.

The first step of energy reconstruction in LArTPC detectors involves the extraction of charge information from the signals (waveforms) on the anode plane wires. The MicroBooNE experiment [1] uses several signal processing techniques [2, 3] including noise filtering and signal deconvolution for charge extraction. However, the total charge extracted in this way normally does not equal the total charge produced from ionization for a number of reasons. The reasons are distortions in detector response due to misconfigured or cross-connected TPC channels [4], space charge effects (SCE) [5], electron attenuation [6–10], diffusion [11] and recombination [12, 13]. To trace back the exact amount of charge released from the original interaction, we have to correct for each of these effects starting from the ionization charge per unit length in the direction of the particle’s travel,  $dQ/dx$ .

The data-driven detector calibration consists of several steps. In the first step we correct the position- and time-dependence of the detector response to ionization charge using data from cosmic ray muons (CR) which enter the detector from either the anode or cathode side and exit through the opposite face (“crossing CR”). This correction process is known as the  $dQ/dx$  calibration of the detector. Once the detector response is corrected to be uniform throughout the TPC and in time, we determine a calibration for converting the ionization charge per unit length,  $dQ/dx$ , to particle energy loss per unit length,  $dE/dx$ , by using “stopping muons from neutrino interactions”. Here stopping muons from neutrino interactions refers to the muons born in the charged current interactions of neutrinos which ultimately decay inside the detector with a Bragg peak in their  $dE/dx$  profile. This process is known as the overall  $dE/dx$  calibration of the detector. In the last step, stopping protons from neutrino interactions are used to further refine the relation between the measured charge and the energy loss for highly ionizing particles.

The MicroBooNE coordinate system is shown in figure 1 (left):  $x$  is the drift direction, and the anode wires are parallel to the  $yz$  plane. The TPC signal formation in MicroBooNE is illustrated in figure 1 (right), where the induction wire planes are referred to as the “U” and “V” planes and the collection wire plane is referred to as the “Y” plane [2]. In this analysis we focus on calibrating only the collection wire plane of the detector, as this is the wire plane predominantly used for calorimetry in a LArTPC. The calibration of induction planes is generally more difficult because the response of the induction wires is highly dependent on the angle of the tracks relative to the wires. New techniques are being developed to improve the reconstruction of the induction plane signals [2, 3], which will allow reliable  $dE/dx$  measurements on induction plane wires in the future.

The two-step calibration procedure is motivated by the similar calibration techniques developed

for other calorimeters such as the MINOS detectors [14].

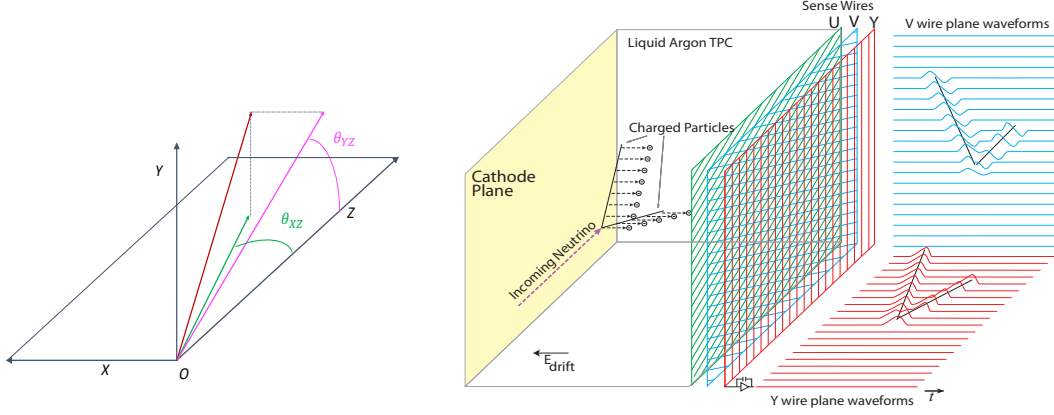


**Figure 1.** (Left) Definition of coordinates  $x$ ,  $y$ , and  $z$ , and the angles  $\theta_{XZ}$  and  $\theta_{YZ}$  of MicroBooNE Detector.  $x$  is along the drift direction with the anode at  $x = 0$  cm and the cathode at 256 cm;  $y$  is in the vertical direction with  $y = -116$  cm at the bottom of TPC and  $y = 116$  cm at the top of TPC;  $z$  is along the beam direction with  $z = 0$  cm at the upstream edge of TPC and  $z = 1036$  cm at the far end. (Right) Diagram illustrating the signal formation in a LArTPC with three wire planes [1]. U wire plane waveforms are similar to that of V wire plane and do not show in the diagram.

## 2 $dQ/dx$ Calibration

### 2.1 Introduction

The goal of the  $dQ/dx$  calibration procedure is to make the detector response uniform in space and over time. There are many effects that can produce a non-uniform detector response. The dominant effects are described in the following sections.

#### 2.1.1 Misconfigured or cross-connected TPC channels

There are several identified issues with the MicroBooNE electronics and wire planes that can affect the TPC response to ionization signals. These effects include ASIC misconfiguration of analog preamplifiers [15], which can change the gain of certain electronic channels, and cross-connected wires, which can distort the electric field between wire planes. Together, these two issues affect roughly 10% of the channels in MicroBooNE. As a consequence, the TPC response has a dependence on the location of charge deposition in the TPC, which needs to be corrected. Figure 2 shows the effect of misconfigured or cross-connected TPC channels on  $dQ/dx$  values.

#### 2.1.2 Space charge effects (SCE)

Since MicroBooNE is a surface-based detector, there is a significant flux of CR tracks in the detector volume. Because of this, there is a significant accumulation of slow-moving positive argon ions inside the detector, which is enough to distort the uniformity of the drift electric field. These distortions in the electric field inside the TPC have two significant effects:

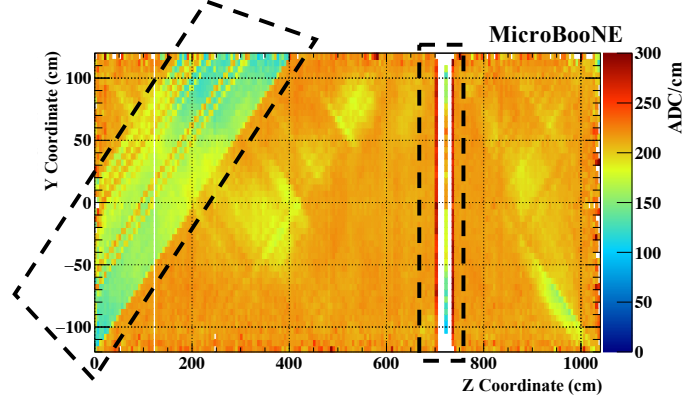


**Figure 2.** Variation of  $dQ/dx$  in the  $yz$  plane in data due to various detector-specific effects such as misconfigured or cross-connected TPC channels, space charge effects, etc in the collection plane. The region inside the highlighted boundaries shows the effect of misconfigured or cross-connected TPC channels. The highlighted diagonal region represents a known region where induction (U) plane channels are interconnected with other induction (V) plane channels [3]. The colors in the plot represent the median  $dQ/dx$  value for a given  $5\text{ cm} \times 5\text{ cm}$  cell in the  $yz$  plane.

- distortions in the magnitude of the drift electric field compared to a uniform E field, and
- distortions in the E field direction compared to the nominal direction parallel to the x-axis.

When the magnitude of the electric field is non-uniform, the recombination of electrons and ions is affected. This recombination effect [12] is sensitive to changes in the electric field. When the drift electric field is relatively low, recombination becomes dominant compared to the recombination at higher electric fields. Moreover, space charge effects can lead to spatial distortions in the trajectories of reconstructed particle tracks and electromagnetic showers. The positive argon ions built up in the detector tend to drag ionization electrons closer to the middle of the detector. The space charge effects are expected to be stronger at the detector edges transverse to the drift direction. The cumulative effect of the space charge in track reconstruction leads to squeezing of the reconstructed track in transverse directions and bending towards the cathode. See Figure 3.

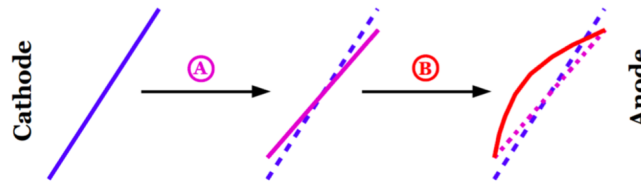


**Figure 3.** Diagram showing the effects of space charge on track reconstruction. The impact is two-fold: the reconstructed track could be squeezed by two extremes in the transverse directions of the TPC, as indicated in the rotation A, and bent towards cathode, as indicated by transformation B. (Image from Ref. [5] used by permission of its creator.)

Figure 4 shows how space charge effects [5] implemented in the MicroBooNE simulation change  $dQ/dx$  values over the entire drift distance of the MicroBooNE LArTPC. As seen in the right plot of figure 4, the  $dQ/dx$  values closer to the cathode are higher compared to that at the anode. The accumulation of positive ions causes the electric field magnitude closer to the cathode to be approximately 10% higher than at the anode. The higher field suppresses electron-ion recombination near the cathode. In addition, due to spatial distortions, tracks reconstructed closer to the cathode are bent and squeezed making reconstructed  $dx$  values smaller. Thus we observe a higher collected charge per unit track length closer to the cathode.

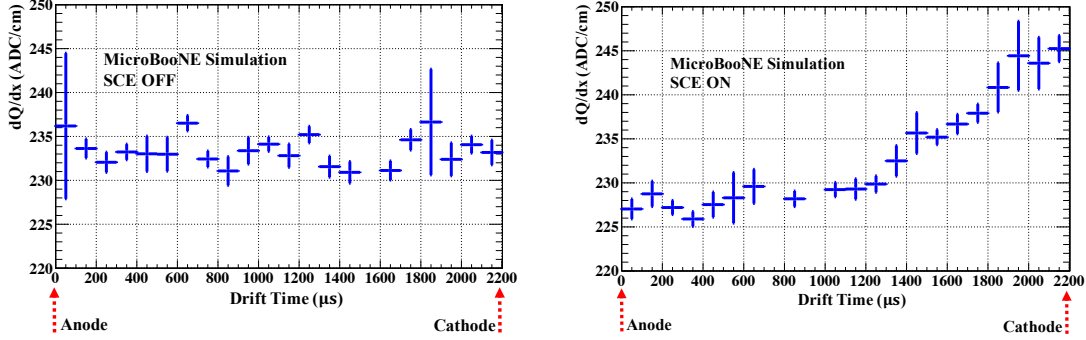


**Figure 4.** Plots of  $dQ/dx$  vs drift distance (time) generated using Monte Carlo (MC) samples of isotropic single muons. (Left) Space charge effects are turned off. (Right) Space charge effects are turned on. In both of the samples diffusion is completely turned off and the electron lifetime is set very high. The plots show how  $dQ/dx$  changes over drift distance when a cloud of ionization electrons drifts from the cathode to the anode with and without space charge effects. Both plots are created using collection plane information and the uncertainties shown are statistical.

### 2.1.3 Electron attenuation

When a cloud of ionization electrons drifts to the anode, electronegative contaminants such as  $H_2O$  and  $O_2$  can capture some of the drifting electrons, reducing the final  $dQ/dx$  measured at the wire planes. The capture rate is dependent on the strength of the applied electric field, as at higher electric field magnitude, ionization electrons have a greater chance of making it to the anode plane before attaching to electronegative impurities.

Equation 2.1 describes the depletion of a cloud of ionization electrons due to capture by electronegative contaminants as the electrons drift towards the anode:

$$\frac{n_e(t_{\text{collected}})}{n_e(t_0)} = \exp\left(\frac{-(t_{\text{collected}} - t_0)}{\tau}\right), \quad (2.1)$$

where  $t_0$  is the start time,  $n_e(t_0)$  is the initial number of electrons at time  $t_0$ ,  $n_e(t_{\text{collected}})$  is the number of electrons collected by anode plane wires after a time  $t_{\text{collected}}$  and  $\tau$  is the electron lifetime.

The electron lifetime depends on the amount of electronegative contaminants present in the medium, where higher electron lifetime corresponds to lower argon contamination levels. Figure 5 shows the effect of electron attenuation on final  $dQ/dx$  values under different purity conditions.

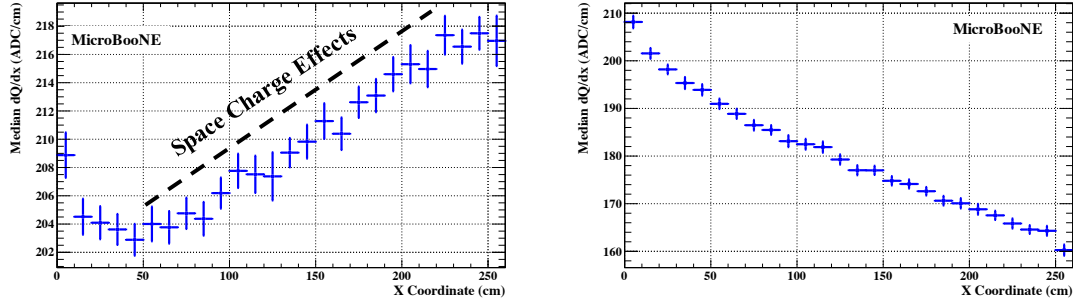


**Figure 5.**  $dQ/dx$  as a function of drift distance under different purity conditions in MicroBooNE data. Here the median  $dQ/dx$  value is plotted for 10 cm wide bins in drift direction on the collection plane. (Left)  $dQ/dx$  as a function of drift distance in high argon purity conditions, with free electron lifetime exceeding 20 ms, on the date Feb-25-2016. In high argon purity conditions space charge effects become dominant, causing  $dQ/dx$  to increase from anode to cathode. (Right)  $dQ/dx$  as a function of drift distance in low argon purity conditions, corresponding to the date March-31-2016, when purity was unusually low (see Figure 9). Here,  $dQ/dx$  value drops from the anode to the cathode due to electron attenuation. This is due to the fact that electronegative contaminants are capturing ionization electrons.

#### 2.1.4 Diffusion

Both longitudinal and transverse diffusion can be studied. The cloud of ionization electrons tends to get smeared out in the direction of the drift because of longitudinal diffusion. This widens and lowers the pulse height of the signal at longer drift distance, which can lead to loss of signal if the pulse-height is below reconstruction threshold. In addition, due to transverse diffusion charge can be detected on multiple wires, which can smear the detected signal and reduce the resolution of charge reconstruction. Diffusion is not a big effect because the electronics shaping time is selected to be comparable to the diffusion smearing.

#### 2.1.5 Temporal variations

The detector response can change over time because of effects such as drift of the electronics gains, changes in temperature, different running conditions, etc. Note the time referred to here is the calendar time, not to be confused with drift time in the TPC. The most significant time-dependent change affecting MicroBooNE calibrations are changes in argon purity.

#### 2.1.6 $dQ/dx$ variation

The general strategy of the  $dQ/dx$  calibration is to separate detector nonuniformities into yz plane, x (drift) direction, and calendar time variations, and calibrate them in sequence using CR. More details will be discussed in section 2.4.

CR are the standard candle for uniform energy deposition throughout the detector. These CR have typical momenta in the range of 4 - 5 GeV, which results in a peak  $dE/dx$  of  $\sim 1.7$  MeV/cm.

It should be noted that the calibration scheme described here is an approximation because contributions such as space charge effects cannot be completely factorized in separate yz plane and drift directions: for a given x value, the variations in the yz plane are different. Ideally we should carry out this calibration by voxelizing the detector into small three-dimensional cubes and derive a



calibration constant for each cube. But limited statistics make the voxelation approach impractical. Moreover, spatial distortions introduced by space charge effects that impact track reconstruction would not be completely addressed by such a voxel-based calibration scheme.

## 2.2 Event selection

As described in section 1, CR are used for the  $dQ/dx$  calibration and stopping muons from neutrino interactions are used for the  $dE/dx$  calibration.

For the  $dQ/dx$  calibration of the detector, we choose to use the anode-cathode crossing CR. The main reason is that the anode-cathode crossing CR span the entire drift distance, which make them a very valuable sample to study any effects that depend on the drift distance. Each CR in the selection is “tagged” with an initial time  $t_0$ , corresponding to the time that the electrons produced nearest the anode are detected. Crossing CR have a wide spatial but limited angular coverage. Figure 6 shows an example of anode-cathode crossing CR in MicroBooNE data and figure 7 shows the x projected track length distribution of all CR.

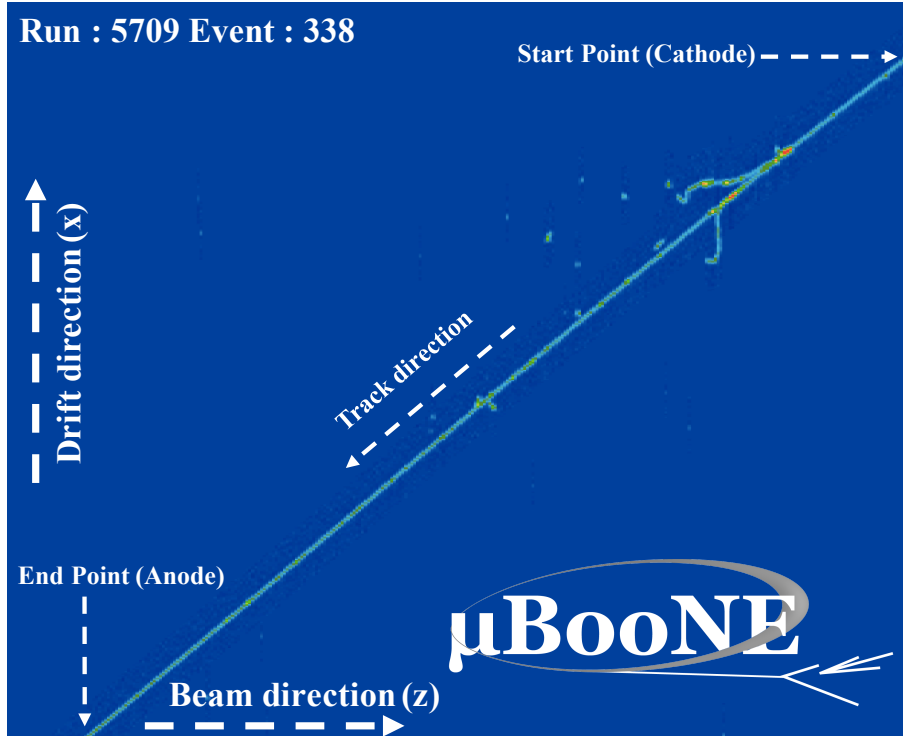


**Figure 6.** An event display showing examples of anode-cathode crossing CR.

The tracks used in the  $dQ/dx$  calibration satisfy the following selection criteria:

- $250 \text{ cm} < \text{Track projected x length} < 270 \text{ cm}$ : Any track that satisfies this selection cut is considered to be an anode-cathode crossing CR. A 20 cm wide window is selected in order to account for imperfect reconstruction of track start and end positions.

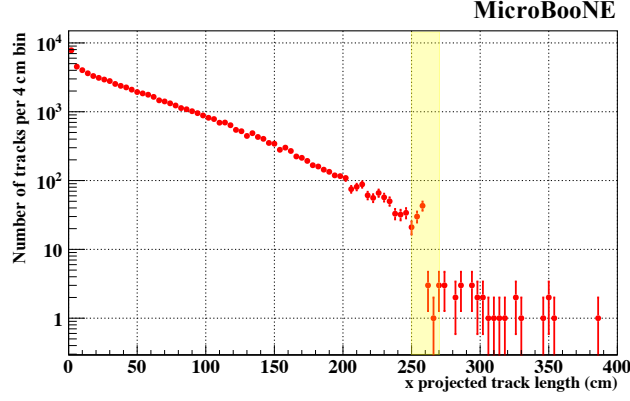


**Figure 7.** Here X axis represents the x projected track length of tracks and Y axis represents number of entries. The colored band shows the x projected track length of anode-cathode crossing CR in MicroBooNE data. It has been estimated that  $\sim 0.13\%$  of the tracks are anode-cathode crossing CR (out of total of 69429 tracks, 87 are crossing CR). The 20 cm width window (in yellow) is selected as anode-cathode crossing tracks to account for to account for mis-reconstruction in track start and end points.

- The absolute value of track angle  $\theta_{XZ}$  (see figure 1) should not be in the range of  $75^\circ$  to  $105^\circ$ : This selection ensures that we are excluding tracks which are nearly orthogonal to the wire planes, which can be mis-reconstructed [2]. See figure 8.
- The absolute value of track angle  $\theta_{YZ}$  (see figure 1) should not be in the range of  $80^\circ$  to  $100^\circ$ : This selection helps to remove tracks that are nearly parallel to the collection plane wires. See figure 8. The difference between Monte Carlo (MC) and data in these figures is due to the fact that the MC simulation does not include detector effects such as space charge effects and the wire field response, perfectly.

### 2.3 Data sample

The  $dQ/dx$  calibration of the detector is carried out using both data and MC simulation. For MC simulation we use samples of simulated CORSIKA CR events [16] overlaid with neutrino interactions simulated with the GENIE generator [17]; for data, we use data collected in the MicroBooNE detector with a trigger coincident with the beam and with a random trigger anti-coincident with the beam from February to October of 2016, and a second period from September 2017 to March 2018. In both MC and data we use the Pandora [18] pattern recognition program, combined with a Kalman filter to fit the CR tracks. We then select only the anode-cathode crossing CR for  $dQ/dx$  calibration.

### 2.4 Analysis method

The  $dQ/dx$  calibration of the detector is carried out in three separate steps for the collection plane.

- Step 1: Detector calibration in the yz plane. This step aims to remove the effects of space charge, misconfigured or cross-connected anode plane channels, and transverse diffusion.

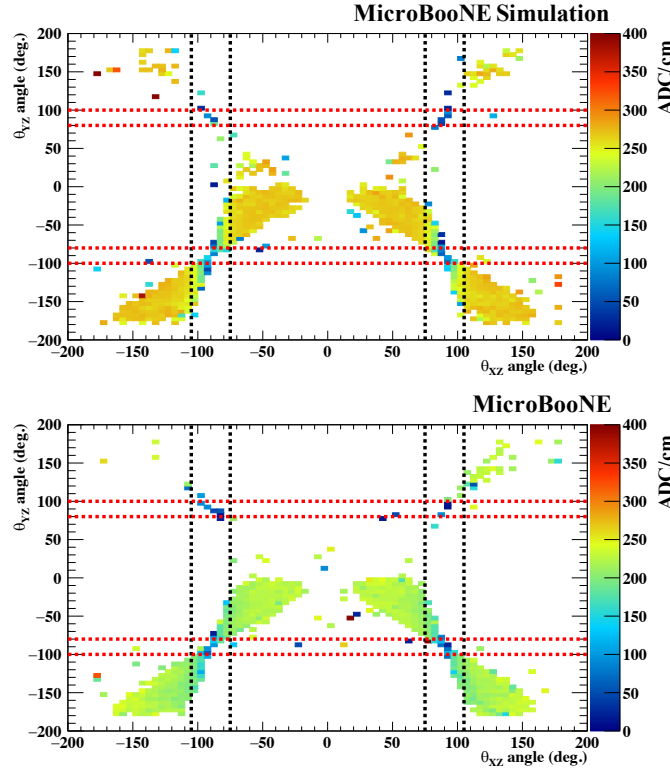


**Figure 8.** Average  $dQ/dx$  values in the phase space of  $\theta_{XZ}$  and  $\theta_{YZ}$  in the collection plane. The color scale represents average  $dQ/dx$  for a track which has a given  $\theta_{XZ}$  and  $\theta_{YZ}$  angular orientation. The units of the Z axis (color scale) are in ADC/cm. Bin size used is  $5^0 \times 5^0$ . The regions inside the dashed lines show the angles excluded for crossing CR tracks as discussed in section 2.2 for the collection plane. (Top) MC. (Bottom) Data.

- Step 2: Detector calibration in the drift (x) direction. This step removes effects of electron attenuation, space charge, and longitudinal diffusion.
- Step 3: Detector calibration in time. This step aims to remove any temporal variations in the detector response. This step is only performed for data. There is currently no time dependence in the MC simulation.

#### 2.4.1 Procedure for detector calibration in the yz plane

Once we have a sample consisting of anode-cathode crossing CR tracks, we use the following procedure to determine the  $dQ/dx$  calibration in the yz plane:

- Isolate crossing CR tracks identified by the selection in section 2.2.
- Calculate starting time ( $t_0$ ); for crossing CR the minimum drift coordinate corresponds to  $t_0$  times the ionization drift velocity.
- Calculate the drift coordinate  $x_{Corrected}$  of each three-dimensional (3D) space point on the track using the  $t_0$  (i.e.,  $x_{Corrected} = x_{Uncorrected} - \text{drift velocity} \times t_0$ ).

- (iv) Segment the  $yz$  plane into 5 cm by 5 cm cells.
- (v) Group each 3D point into its relevant cell in  $yz$  using the  $y$  and  $z$  coordinates that satisfy the conditions  $0 \text{ cm} < x_{Corrected} < 260 \text{ cm}$ ,  $-120 \text{ cm} < y < 120 \text{ cm}$ , and  $0 \text{ cm} < z < 1040 \text{ cm}$ .
- (vi) After looping over all crossing CR tracks, only keep cells which have at least five 3D track points.
- (vii) For each of the selected cells, we calculate a median  $dQ/dx$  value by considering charge information of all the 3D points in that cell. The median  $dQ/dx$  of a given cell is called the “local median  $dQ/dx$ ” of that cell (median  $dQ/dx$  is chosen to remove delta ray contamination and misreconstructed calorimetric information).
- (viii) Calculate the “global median  $dQ/dx$ ” by taking the median  $dQ/dx$  value from all the 3D points coming from all crossing tracks. This median is taken over all non-empty cells as well.
- (ix) For each cell in the  $yz$  plane, define a correction factor  $C(y_i, z_i)$  using;

$$C(y_i, z_i) = \frac{(dQ/dx)_{Global}}{((dQ/dx)(y_i, z_i))_{Local}}. \quad (2.2)$$

#### 2.4.2 Procedure for detector calibration in the drift direction

After calibrating the  $yz$  plane, we next move to the drift direction calibration of the detector. The following explains how this calibration procedure is carried out:

- (i) Isolate crossing CR tracks and calculate the drift coordinate  $x_{Corrected}$  of each three-dimensional (3D) space point on tracks as in the procedure for  $yz$  plane calibration.
- (ii) Correct the charge information ( $dQ/dx$ ) of each 3D point using  $yz$  correction factors, derived in the previous step, to remove the irregularities in the  $yz$  plane using equation 2.3. If cells do not have a minimum of five 3D track points,  $yz$  correction factors of nearby cells are used to correct the charge information. Here we select the 3D points that satisfy  $0 \text{ cm} < x_{Corrected} < 260 \text{ cm}$ ,  $-120 \text{ cm} < y < 120 \text{ cm}$ , and  $0 \text{ cm} < z < 1040 \text{ cm}$ . Moreover we examine the  $y$  and  $z$  coordinates of the 3D point to determine which  $yz$  correction factor to use.

$$((dQ/dx)(y_i, z_i))_{Corrected} = C(y_i, z_i) \cdot ((dQ/dx)(y_i, z_i))_{Reconstructed}, \quad (2.3)$$

where  $((dQ/dx)(y_i, z_i))_{Corrected}$  is the corrected  $(dQ/dx)$  value by  $C(y_i, z_i)$  correction factor for irregularities in the  $yz$  plane, and  $((dQ/dx)(y_i, z_i))_{Reconstructed}$  is the uncorrected  $dQ/dx$  value.

- (iv) Segment the drift direction into bins of 10 cm in data and bins of 5 cm in MC. Bin sizes are chosen to minimize statistical fluctuations in the correction factors.
- (v) Group each 3D point into the relevant drift direction bin based on its corrected  $x$  coordinate.

- (vi) Define a “local median  $dQ/dx$ ” for each of the bins in the drift direction which has more than five 3D points.
- (vii) Define “global median  $dQ/dx$ ” as explained in the previous calibration procedure.
- (viii) for each bin in the drift direction, a correction factor  $C(x_i)$  is defined using equation 2.4;

$$C(x_i) = \frac{(dQ/dx)'_{Global}}{((dQ/dx)(x_i))'_{Local}}, \quad (2.4)$$

where  $(dQ/dx)'_{Global}$  is the global median  $dQ/dx$  value after correcting for yz plane irregularities by equation 2.3 in the collection plane, and  $((dQ/dx)(x_i))'_{Local}$  is the local  $dQ/dx$  median for the given  $x_i$  position after correcting for yz plane irregularities by equation 2.3 in the collection plane.

In data, we derive the drift direction correction factors for each day as space charge effects and electron lifetime can change over time. To get a reliable set of correction factors, we need a data sample which contains enough statistics. For this purpose, we derive correction factors in the drift direction only for the days where there are more than 40 crossing tracks after all the angular cuts. In the case of lack of statistics for a given day, we use the drift direction correction factors derived for the immediate neighboring day. For MC we derive only a single set of drift direction correction factors for the collection plane as there is no time variation of space charge effects and electron attenuation.

#### 2.4.3 Procedure for time dependent calibration of the detector

Next, temporal variations in the detector response are addressed. The following set of steps explains how the detector calibration in time is achieved:

- (i) Select tracks and hits as described in sections 2.4.1 and 2.4.2.
- (ii) Correct  $dQ/dx$  value of each 3D track point using correction factors derived for the yz plane and drift direction using equation 2.5 by looking into the corrected  $x, y$ , and  $z$  coordinates.
- (iii) Calculate a “global median  $dQ/dx$ ” value by taking the median  $dQ/dx$  value of all the hits in the entire TPC volume for the day, we want. In the time calibration of the detector, we calculate this global median  $dQ/dx$  value on a daily basis.
- (iv) Plot the global median  $dQ/dx$  values against time to visualize the detector variations in time (See figure 9).
- (v) Choose the reference value (210 ADC/cm) for the global median  $dQ/dx$  in the collection plane, since all global median  $dQ/dx$  values calculated for each day fluctuate around this value. See figure 9.
- (vi) Determine a time dependent correction  $C(t)$  using equation 2.6 for each day.

$$((dQ/dx)(x_i, y_i, z_i))_{Corrected} = C(y_i, z_i) \cdot C(x_i) \cdot ((dQ/dx)(x_i, y_i, z_i))_{Reconstructed}, \quad (2.5)$$

where  $((dQ/dx)(x_i, y_i, z_i))_{Corrected}$  is the corrected  $dQ/dx$  value for yz plane and drift direction irregularities in the collection plane, and  $((dQ/dx)(x_i, y_i, z_i))_{Reconstructed}$  is the uncorrected  $dQ/dx$  value in the collection plane.

$$C(t) = \frac{(dQ/dx)_{Reference}}{((dQ/dx)(t))_{Global}}, \quad (2.6)$$

where  $(dQ/dx)_{Reference}$  is the reference  $dQ/dx$  value in the collection plane, and  $((dQ/dx)(t))_{Global}$  is the global  $dQ/dx$  value in the collection plane after correcting for yz plane and drift direction irregularities for each day.

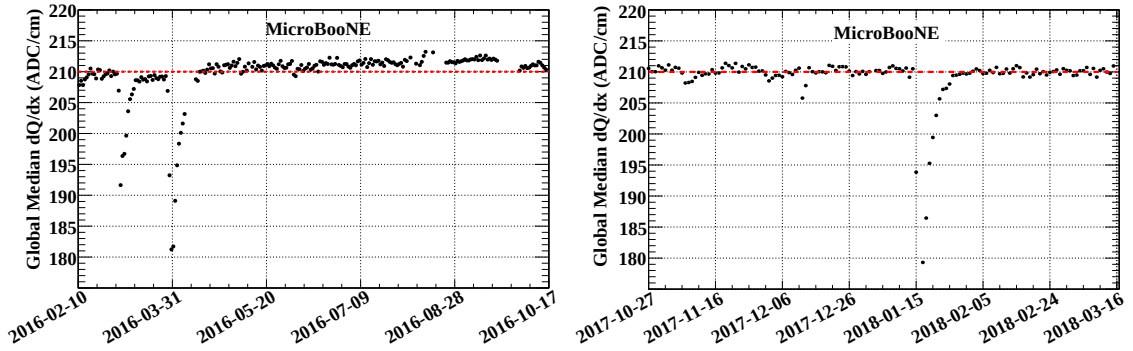


**Figure 9.** The global median  $dQ/dx$  per day over time in the collection plane. The red lines drawn shows the reference value selected which is 210 ADC/cm. Left: the global median  $dQ/dx$  from February 10, 2016 to October 17, 2016 in run period I. Right: the global median  $dQ/dx$  from October 27, 2017 to March 16, 2018 in run period III. Dips from the reference values across several days are due to time periods in which argon purity was low (e.g. during recirculation pump maintenance).

Once we are finished with calibrating the detector in the yz plane, drift direction, and in time, we can use equation 2.7 and equation 2.8 to compute the calibrated  $dQ/dx$  values in data and MC, respectively.

$$((dQ/dx)(x_i, y_i, z_i, t))_{Corrected}^{data} = ((dQ/dx)(x_i, y_i, z_i, t))_{Reconstructed} \cdot C(y_i, z_i) \cdot C(x_i) \cdot C(t), \quad (2.7)$$

where  $((dQ/dx)(x_i, y_i, z_i, t))_{Corrected}^{data}$  is the corrected  $dQ/dx$  for yz plane, drift direction irregularities and time variations in data in the collection plane, and  $((dQ/dx)(x_i, y_i, z_i, t))_{Reconstructed}$  is the uncorrected  $dQ/dx$  in data in the collection plane.

$$((dQ/dx)(x_i, y_i, z_i))_{Corrected}^{MC} = ((dQ/dx)(x_i, y_i, z_i))_{Reconstructed} \cdot C(y_i, z_i) \cdot C(x_i), \quad (2.8)$$

where  $((dQ/dx)(x_i, y_i, z_i))_{Corrected}^{MC}$  is the corrected  $dQ/dx$  for yz plane and drift direction irregularities in MC in the collection plane, and  $((dQ/dx)(x_i, y_i, z_i))_{Reconstructed}$  uncorrected  $dQ/dx$  in MC in the collection plane.

## 2.5 Results

### 2.5.1 $dQ/dx$ calibration (Simulation)

The  $dQ/dx$  calibration of the detector in MC is performed using a single large dataset described in section 2.3. Figure 10 shows the extracted  $yz$  correction factors  $C(y, z)$  and drift direction  $x$  correction factors  $C(x)$ .

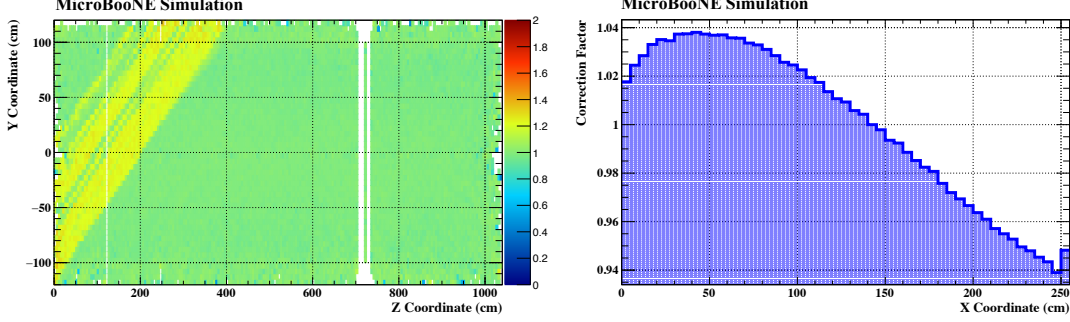


**Figure 10.** Left:  $yz$  correction factors in the collection plane in MC. Here the  $Z$  axis color represents correction factors for a given  $5\text{ cm} \times 5\text{ cm}$  cell in the  $yz$  plane. Right: Drift direction correction factors in MC simulation. Here the variation of these correction factors w.r.t drift direction could be attributed to electron attenuation as well as space charge effects.

### 2.5.2 $dQ/dx$ calibration (data)

The  $yz$  and drift direction  $x$  correction factors are derived for two separate datasets as described in section 2.3. In the first dataset, we have data combined from February 2016 to October 2016; and in the second dataset, we have data combined from September 2017 to March 2018. See figure 11 and figure 12 for the variation of the  $yz$  correction factors and drift direction  $x$  correction factors in the collection plane for the two datasets.

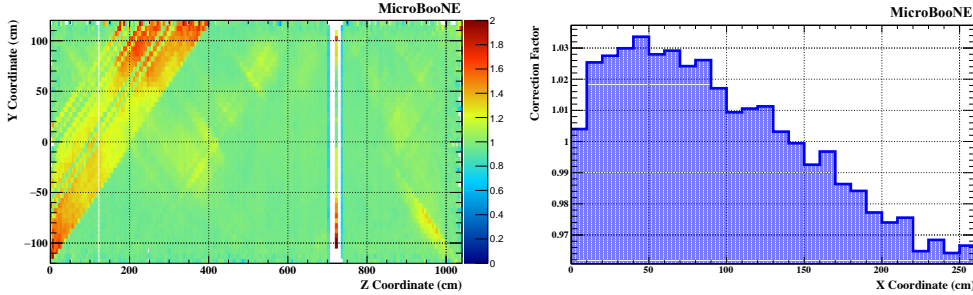


**Figure 11.** Left:  $yz$  correction factors for data taken in from February to October in 2016. Here the  $Z$  axis color represents correction factors for a given  $5\text{ cm} \times 5\text{ cm}$  cell in the  $yz$  plane. Right: A set of drift direction  $x$  correction factors (Feb-25-2016) for data taken in from February to October in 2016.

The drift direction corrections factors and time corrections are derived for the time period from February 2016 to October 2016 and the time period from September 2017 to March 2018.  $C(t)$  is calculated for each day. Due to intermittent periods of detector downtime, some days are skipped

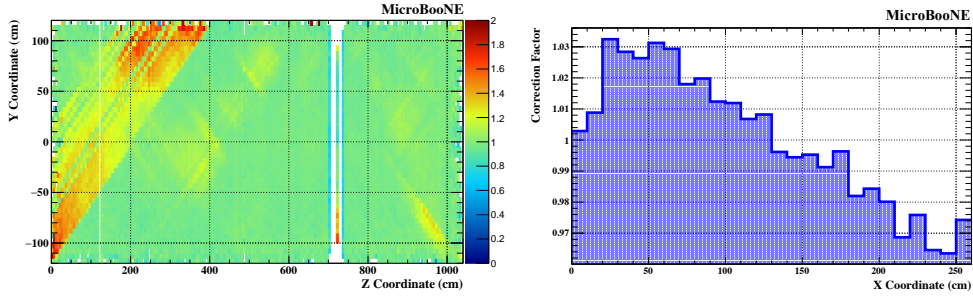


**Figure 12.** Left: yz correction factors for data taken in from September 2017 to March in 2018. Here the Z axis color represents correction factors for a given  $5\text{ cm} \times 5\text{ cm}$  cell in the yz plane. Right: A set of drift direction x correction factors (Jan-14-2018) for data taken in September 2017 to March in 2018.

in this measurement. See figure 13 for the variation of the time-dependent correction factor over time. Figure 14 shows the impact of the  $dQ/dx$  calibration on the  $dQ/dx$  distribution in both MC and data. The resolution of  $dQ/dx$  is clearly improved. Quantitatively, after the  $dQ/dx$  calibration, the widths of the  $dQ/dx$  distributions have narrowed by 2% for both MicroBooNE data and MC.

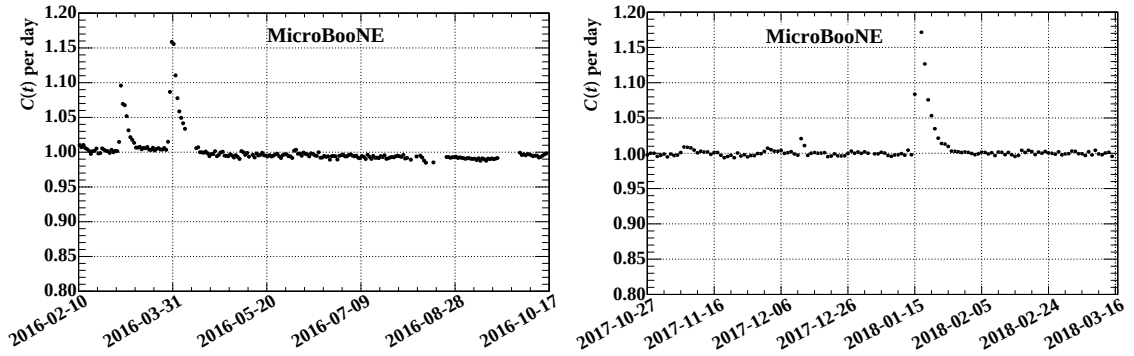


**Figure 13.** Left: The time correction  $C(t)$  shown for data taken from February 2016 to October 2016. Right: The time correction  $C(t)$  shown for data taken from September 2017 to March 2018.

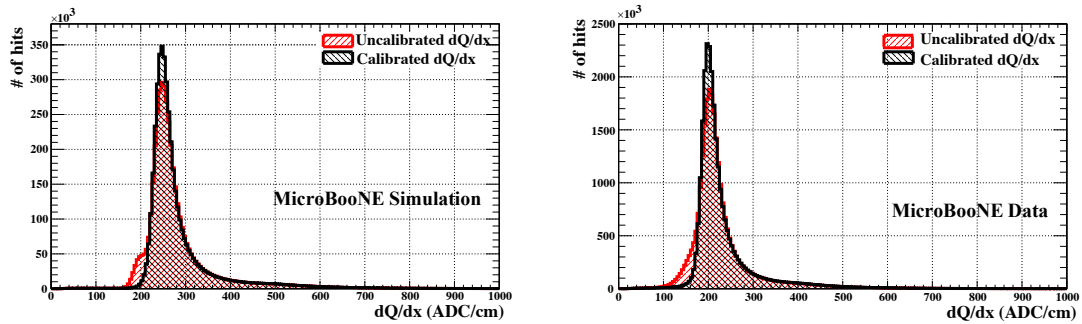


**Figure 14.** Left: Calibrated and uncalibrated  $dQ/dx$  in simulation using crossing CR in the collection plane. Right: Calibrated and uncalibrated  $dQ/dx$  in data using crossing CR in the collection plane. In these plots the Y-axis label # of hits refers to the number of 3D trajectory points of tracks.



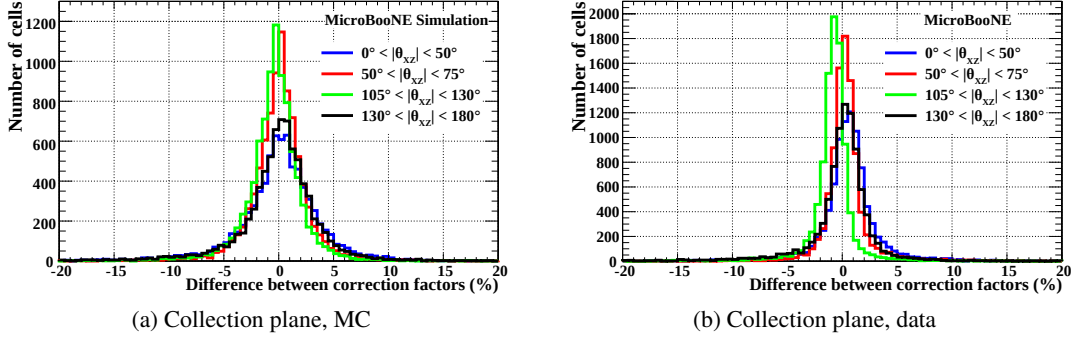


**Figure 15.** Relative differences of the yz correction factors for each angular subsample with respect to the complete sample, as defined in text.

## 2.6 Angular dependence study

The calibration procedure described in this paper does not make any angular-dependent corrections because of the limited angular coverage of anode-cathode crossing CR. The angular distributions of the anode-cathode crossing CR tracks are shown in figure 8. In order to more closely study the angular dependence of the  $dQ/dx$  calibration, we divide the crossing CR into four angular subsamples:

- $0^\circ < |\theta_{XZ}| < 50^\circ$ ,
- $50^\circ < |\theta_{XZ}| < 75^\circ$ ,
- $105^\circ < |\theta_{XZ}| < 130^\circ$  and
- $130^\circ < |\theta_{XZ}| < 180^\circ$ .

and derive the yz and x correction factors for each subsample following the same procedure described above. All of the other selection criteria remain the same.

For each yz cell in each subsample, we compute the relative difference of the yz correction factor for the subsample  $C_{\text{subsample}}(y_i, z_i)$  from the correction factor found using all crossing CR  $C(y_i, z_i)$ . Figure 15 shows the distribution of the relative differences of the yz correction factors relative to the complete sample,  $[C_{\text{subsample}}(y_i, z_i) - C(y_i, z_i)] / C(y_i, z_i)$ , for each angular subsample. The shift in the mean of the distribution away from zero is indicative of the amount of bias observed in a given angular bin. The peaks of the four distributions all agree within 2%.

Figure 16 shows the relative differences in the x correction factors between the different angular subsamples and the combined sample. The maximum variation is 1.5%.

Based on the above studies, we assign a 2% systematic error on the yz correction and a 1.5% systematic error on the x correction for the collection plane. This study shows very little angular dependence for the sample selected for the  $dQ/dx$  calibration. However, because of the limited angular coverage of this sample, more studies are underway to further refine the angular dependence of the detector response.

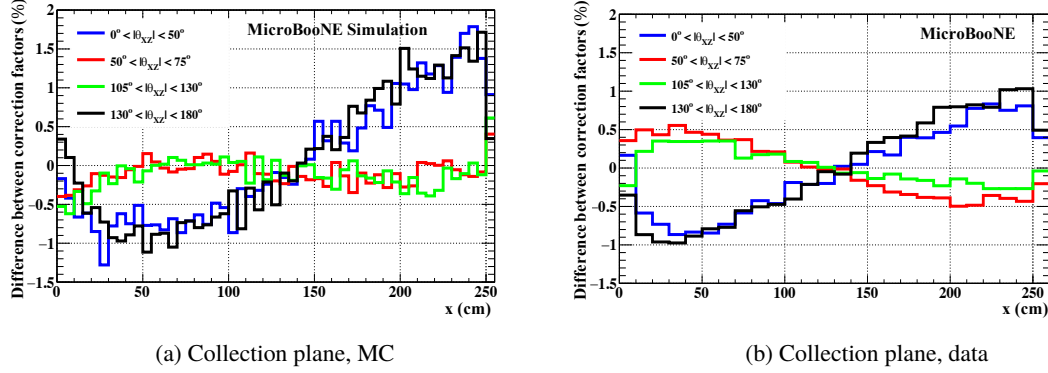


**Figure 16.** Relative differences in  $x$  correction factors between different angular subsamples and the combined sample. The differences between simulation (left) and data (right) could be due to a mis-modeling of space charge effects or wire response in our simulation.

### 3 $dE/dx$ Calibration

#### 3.1 Introduction

After the  $dQ/dx$  correction is complete we can determine the absolute energy scale. To move from the calibrated  $dQ/dx$  to  $dE/dx$ , we use the modified box model [12] for recombination:

$$\left(\frac{dE}{dx}\right)_{calibrated} = \frac{\exp\left(\frac{(\frac{dQ}{dx})_{calibrated}}{C_{cal}} \frac{\beta' W_{ion}}{\rho \mathcal{E}}\right) - \alpha}{\frac{\beta'}{\rho \mathcal{E}}}, \quad (3.1)$$

with

$C_{cal}$  is a calibration constant used to convert ADC values to number of electrons,

$$\begin{aligned} W_{ion} &= 23.6 \times 10^{-6} \text{ MeV/electron (work function of argon),} \\ \mathcal{E} &= 0.273 \text{ kV/cm (MicroBooNE drift electric field),} \\ \rho &= 1.38 \text{ g/cm}^3 \text{ (liquid argon density at a pressure 124.106 kPa),} \\ \beta' &= 0.212 \text{ (kV/cm)(g/cm}^2\text{)/MeV, and} \\ \alpha &= 0.93. \end{aligned}$$

The last two parameters were measured by the ArgoNeuT experiment [12] at an operational electric field of 0.481 kV/cm. The modified box model is applied at MicroBooNE’s electric field of 0.273 kV/cm for minimal ionizing particles.

According to the above equation, precise determination of the calibration constant  $C_{cal}$  which translates “ADC/cm” to “(number of electrons)/cm”, is important in determining the absolute energy scale. The charge  $Q$  is measured by the integral of the pulse of the deconvoluted anode response signal where the simulated electronics and field responses are removed.  $C_{cal}$  is normalized so that the unit (“ADC”) corresponds to 200 electrons. In the case where the detector response is perfectly modeled (*e.g.* in the simulation), the calibration constant  $C_{cal}$  should be exactly 1/200. Here the goal of the  $dE/dx$  calibration is to determine the calibration constant  $C_{cal}$  using stopping muons as

the standard candle, because they have a well-understood energy loss profile. A sample of stopping muons can either be identified from cosmic data or neutrino interactions. The method we use for  $dE/dx$  calibration is discussed in section 3.4.

### 3.2 Event selection

In the  $dE/dx$  calibration of the detector, we employ stopping muons induced by neutrino interactions. The motivation is to get a sample of muons from neutrino interactions with known muon energy so that a portion of the track can be selected that corresponds closely to a minimum ionizing particle, for which the  $dE/dx$  is very well understood theoretically to better than 1%. There are several advantages in using this sample. First, our main focus is to calibrate the energy of particles in neutrino interactions and the angular profile of outgoing tracks from neutrino interactions is well represented by these stopping muons. Second, since these stopping muons are mostly forward-going, many collection plane hits can be expected. In addition, the start time of these stopping muons is well known and important in applying the correction factors derived in the  $dQ/dx$  calibrations. The arrival time of the neutrino beam to the detector helps to find the start time of the muons originating from neutrino interactions. We use the following criteria to isolate these muons in MC:

- Select the tracks whose reconstructed start and end point  $x$ ,  $y$  and  $z$  satisfy  $10 \text{ cm} < x < 250 \text{ cm}$ ,  $-110 \text{ cm} < y < 110 \text{ cm}$  and  $10 \text{ cm} < z < 1030 \text{ cm}$ . This ensures that each candidate is well contained within the TPC.
- Match the reconstructed track to a stopping muon that comes from a neutrino interaction using truth information (this applies only to MC).
- Select the tracks that satisfy the distance between start (end) point of the true track and start (end) point of the reconstructed track  $< 5 \text{ cm}$ ; This cut further ensures that we are getting the correct reconstructed muon track (this applies only to MC).
- Apply an angular cut; the absolute value of the reconstructed track angle  $\theta_{xz}$  is not in the range of  $75^\circ$  to  $105^\circ$ . This selection ensures that we are excluding the tracks which are pointing into the wire planes.
- Apply a second angular cut; the absolute value of the reconstructed track angle  $\theta_{yz}$  is not in the range of  $80^\circ$  to  $100^\circ$ . This selection ensures that we are excluding tracks which are nearly parallel to the collection plane wires.

To isolate stopping muons in data, the following selection criteria are applied:

- Select charged current  $\nu_\mu$  interactions with inclusive final states [19].
- Apply the same track containment and angular cuts as applied to the MC sample.
- Calculate the median  $dQ/dx$  values of the track in the first and last 5 cm segments. If the ratio of the median  $dQ/dx$  value in the last 5 cm segment to that of the first 5 cm segment is greater than 1.5, the track is selected as a stopping muon. This cut aims to find the Bragg peak and remove poorly reconstructed tracks. This cut value is determined from a MC simulation sample of well-reconstructed stopping muons. See figure 17.

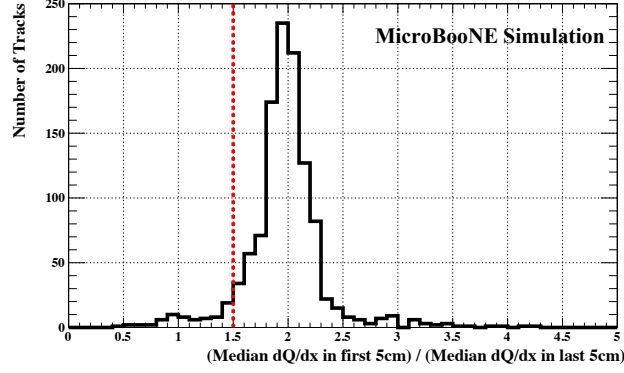


**Figure 17.** Ratio of the  $dQ/dx$  in the last to first 5 cm segment of stopping muons in MicroBooNE simulation. The x axis is the ratio between the median  $dQ/dx$  of first 5 cm of the track and median  $dQ/dx$  of the last 5 cm of the track. The y axis is the number of stopping muon tracks coming from neutrino interactions in MC. We select a cut value of 1.5 for the ratio considered to find well reconstructed stopping muon tracks in data.

### 3.3 Data sample

The  $dE/dx$  calibration of the detector is performed on both MC and data samples. For MC we use a CORSIKA CR simulation overlaid with neutrino interactions to obtain stopping muons induced by the neutrino interactions, where these stopping muons are reconstructed using the Pandora package. In data we use datasets collected from February 2016 to October 2016 and from September 2017 to March 2018 to obtain candidate stopping muons from charged current interactions.

### 3.4 Analysis method

The following explains the procedure to perform the  $dE/dx$  calibration both in MC and data:

- (i) Start with a set of tracks that satisfy the selection in section 3.2.
- (ii) Segment the last 200 cm residual ranges (residual range is defined as the path of the particle before its stopping point) of tracks into 5 cm bins, which leads to a total of 40 residual range bins; here we select tracks that have a minimum track length of 150 cm. The motivation behind the track length threshold serves two purposes. This guarantees that the track is well reconstructed and is minimum ionizing.
- (iii) Loop over all the 3D points of each selected track and fill the residual range bins with  $dE/dx$  values derived using equation 3.1 by setting the the calibration constant  $C_{cal}$  to an arbitrary value; only the 3D points that are inside the detector boundaries specified in section 2.4.1 are considered here. Moreover, we consider only the 3D points which are separated by 0.3 to 0.4 cm; as the minimum spacing between 3D points is set by the wire spacing of 0.3 cm, this selects forward going muons.
- (iv) After looping over all the tracks, fit each  $dE/dx$  distribution to a Landau-convoluted Gaussian function [20] to extract the most probable  $dE/dx$  value (MPV) representing that particular residual range bin.

- (v) Plot the MPV  $dE/dx$  values against the kinetic energy of the particle; for each residual range bin, we take the middle bin value as the representative residual range value of that bin and transform that to kinetic energy. In this transformation we use a cubic spline fit to the tabulated values of CSDA (continuous slowing down approximation) residual range vs. kinetic energy for stopping muons in liquid argon [21].
- (vi) Compare the curve generated in the previous step with the prediction made by the Landau-Vavilov function [22] in the kinetic energy range of the muons from 250 MeV to 450 MeV, which is in the MIP region, and a  $\chi^2$  value is calculated using equation 3.2. The Landau-Vavilov function describes the energy loss probability distribution for a particle in a given medium. The most probable energy loss of a particle is dependent on the thickness of the energy absorber. To get the predicted MPV  $dE/dx$ , we set the absorber thickness to be 0.35 cm, the average value of  $dx$ .
- (vii) Iterate through the steps iii to vi described above several times to generate tabulated set of data between a given calibration constant ( $C_{cal}$ ) and  $\chi^2$  value.
- (viii) In the final step, plot the  $\chi^2$  values generated against calibration constants and fit that distribution with a second order polynomial to get the calibration constant which corresponds to the lowest  $\chi^2$  value.
- (ix) With the newly derived calibration constant ( $C_{cal}$ ), calculate the  $dE/dx$  values using equation 3.1 with calibrated  $dQ/dx$  values as the input.

After the  $dE/dx$  calibration, we compare the newly derived  $dE/dx$  values with uncorrected  $dE/dx$  values to see the effects of applying the algorithm. (See section 3.5).

$$\chi^2 = \sum \left( \frac{(MPV(dE/dx)_{Predicted} - MPV(dE/dx)_{Measured})^2}{\sigma^2} \right), \quad (3.2)$$

where we sum all the data points in the kinetic energy region of 250 MeV to 450 MeV.

For MC,  $\sigma^2 = \delta_{fit}^2$ , where  $\delta_{fit}$  is the uncertainty associated with the MPV  $dE/dx$  extracted by fitting a Landau-convoluted Gaussian function to the energy distribution.

For data,  $\sigma^2 = \delta_{fit}^2 + \delta_{recombination}^2$ , where  $\delta_{recombination}$  is the systematic error associated with recombination model uncertainties (here we take the uncertainty to be 1.5% of the measured  $dE/dx$ . This uncertainty is coming from the  $1\sigma$  level uncertainties of the two free parameters  $\beta'$  and  $\alpha$  in the modified box model for recombination in equation 3.1).

Note the MC sample was simulated and reconstructed with the same recombination model. Therefore, there is no systematic uncertainty associated with the recombination model for MC.

### 3.5 Results

The absolute calibration of the detector is performed on both MC and data samples. Figure 18 shows the comparison between the prediction (from equation 3.1 using the default values) with the fitted MPV  $dE/dx$  using the calibration constants shown in table 1 for stopping muons both in MC and data.

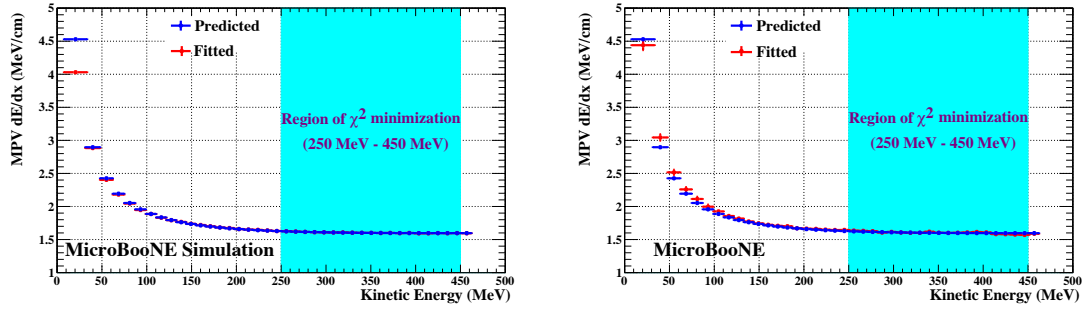


**Figure 18.** (Left) Comparison between the prediction and the fitted MPV  $dE/dx$  for stopping muons in MC using the collection plane. (Right) Comparison between the prediction and the fitted MPV  $dE/dx$  for stopping muons in MicroBooNE data from 2016 using the collection plane. The disagreement between the fitted distribution and theory at lower kinetic energies is mainly due to the recombination model uncertainty. Results can be applied to all time ranges, since temporal variations are taken into account by the relative  $dQ/dx$  corrections. The first data point in the distributions correspond to the end of the tracks. Most of the time the end of the track can happen in between two wires. Therefore calorimetric information for the end points of tracks is not properly reconstructed. The significant deviation between prediction and our fitted distribution for MC in the first bin is due to this reason.

Figure 19 shows  $\chi^2 - \chi_{Min}^2$  vs the calibration constant  $C_{cal}$  for the collection plane. The best fit value is the one that gives the minimal  $\chi^2$ . The uncertainty on the extracted value of  $C_{cal}$  is given by  $\Delta\chi^2 = \chi^2 - \chi_{Min}^2 = 1$ .

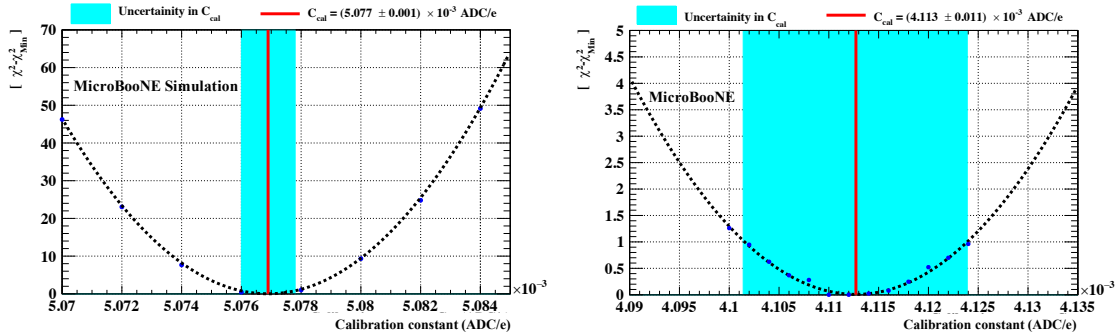


**Figure 19.** Distributions of  $\chi^2 - \chi_{Min}^2$  vs. calibration constant  $C_{cal}$  for the collection plane. The color bands show the uncertainty associated with calibration constant  $C_{cal}$ . (Left) MC. (Right) Data. Results are applicable to all periods of data-taking, as temporal variations are taken into account by the relative  $dQ/dx$  corrections.

The calibration constants derived for the collection plane are shown in table 1. The MC calibration constant uncertainty is statistical only. The data calibration constant uncertainty includes both the statistical uncertainty and the recombination uncertainty. Figure 18 shows the comparison between the prediction and the measured MPV  $dE/dx$  with these calibration constants for stopping muons both in MC and data.

The absolute energy-scale calibration can be validated in a data-driven way by comparing the range-based energy to that obtained via calorimetry for selected stopping muon candidates in data

**Table 1.** Calibration constants and  $\chi^2_{Min}/d.o.f.$  for the collection plane in MC and data.

	MC	Data
Fitted value of $C_{cal}$	$(5.077 \pm 0.001) \times 10^{-3}$ ADC/e	$(4.113 \pm 0.011) \times 10^{-3}$ ADC/e
$\chi^2_{Min}/d.o.f$	15.0/18 $\sim$ 0.84	5.12/18 $\sim$ 0.28

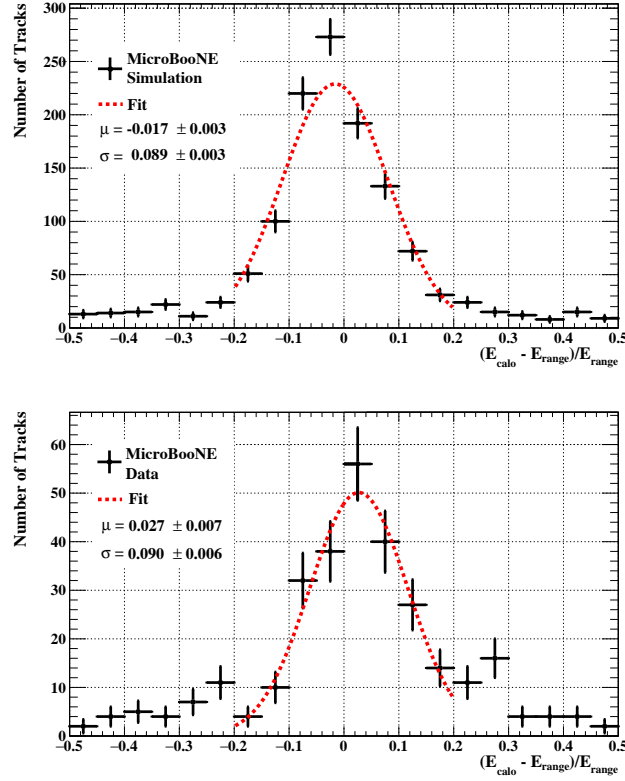


**Figure 20.** Relative difference in range vs. calorimetric kinetic energy for selected stopping muons in MC (top) and data (bottom). The distributions are fit to a Gaussian which returns a mean  $\mu = -0.017 \pm 0.003$  and width  $\sigma = 0.089 \pm 0.003$  for MC and a mean  $\mu = 0.027 \pm 0.007$  and width  $\sigma = 0.090 \pm 0.006$  for data.

and MC. For each selected stopping muon track, the kinetic energy calculated by range and by calorimetry is computed, and the relative difference between these methods is shown in figure 20. Here, in calculating the kinetic energies, the entire track is used. The agreement between the two, approximately 3% for data (2% in MC), gives confidence in the proper absolute energy-scale calibration to within this level of agreement, and provides a closure test for this calibration procedure.

## 4 Energy correction with protons

### 4.1 Introduction

After the detector response has been corrected for the  $dQ/dx$  uniformity and the absolute energy scale has been determined, we perform studies using a proton sample to investigate recombination effects on ionization energy.

The measurements of  $dQ/dx$  and  $dE/dx$  calibration presented in the previous sections determine the energy scale for minimum ionizing particles, but we still need to verify that the  $dE/dx$  measurement is valid for highly ionizing particles. The relation between  $dQ/dx$  and  $dE/dx$  (see eq. 3.1) is not linear and its dependency has been broadly studied [23, 24]. We use protons to measure the non-linear relation between  $dQ/dx$  and  $dE/dx$ . The use of protons is justified since they cover a wider range of energy loss than minimum ionizing particles. In this analysis, we use  $dQ/dx$  in  $(e/cm)$  making use of the conversion obtained in table 1. This relation between  $dQ/dx$  and  $dE/dx$  is impacted by recombination of electron-ion pairs [24] that produces a loss in the charge measured. This effect has to be corrected in order to properly estimate  $dE/dx$ .

For crossing muons, where the energy deposit is constant, the relation between  $dE/dx$  and  $dQ/dx$  is a constant. Variations of the  $dQ/dx$  can be observed as we vary  $dE/dx$ . Since this relation is non-linear, the crossing muon sample has been used to estimate the scale factor for the electronic response (thus the relation between  $dQ/dx$  and  $dE/dx$  when  $dE/dx$  is constant). Then, the sample of protons provides the  $dQ/dx$  dependency over  $dE/dx$ , since the protons cover a larger range in  $dE/dx$  allowing us to study the non-linearity of this relation. Thus, with protons we are able to observe the full recombination curve.

The MC sample used for this analysis has been simulated with the modified box model, with the parameters obtained by the ArgoNeUT experiment [12].  $dQ/dx$  has been reconstructed using the initial simulated  $dE/dx$  following:

$$\frac{dQ}{dx} = \frac{\ln(\frac{dE}{dx} \frac{\beta'}{\rho \mathcal{E}} + \alpha)}{\frac{\beta'}{\rho \mathcal{E}} W_{\text{ion}}}, \quad (4.1)$$

with the parameters  $W_{\text{ion}}$ ,  $\mathcal{E}$ ,  $\rho$ ,  $\beta'$  and  $\alpha$ , already described in the inverse of this equation, see 3.1.

A way to understand whether or not our observations in data agree with the modified box model, or if we need a change in its parametrization, is to perform the same study with a different model. We include studies in this section using the Birks' law, following eq. 4.2 with  $A_B = 0.8$  and  $k = 0.0486 \text{ (kV/cm)(g/cm}^2\text{)/MeV}$ , as measured by the ICARUS collaboration [13]. Since the two models, Birks and modified box, are different but both have a parameter which is fully correlated to the electric field ( $k$  and  $\beta'$  respectively), they can help us to understand if any modification in the model's parameters required by the data can also be explained by distortions on the electric field. Birks' law can be written as:

$$\left(\frac{dQ}{dx}\right) = A_B \left( \frac{\frac{dE}{dx}}{1 + \frac{k}{\mathcal{E}} \frac{dE}{dx}} \right). \quad (4.2)$$

To perform these studies we use the reconstructed  $dQ/dx$  and calculate  $dE/dx$  using an empirical fit to Bethe-Bloch energy loss using the range information,  $dE/dx_{\text{range}}$ . The values of



$dE/dx_{\text{range}}$  are calculated independently using only the residual range information per hit for a proton hypothesis, as described by ArgoNeuT [12] according to eq. 4.3

$$\left(\frac{dE}{dx}\right)_{\text{range}} = A \cdot R^b \quad (4.3)$$

where  $R$  is the range and  $A$  is an empirical constant (the constant  $A$  in eq. 4.3 should not be confused with  $A_B$  from Birks' law in eq. 4.2). We use the values obtained by ArgoNeuT,  $A = 17 \text{ MeV/cm}^{1-b}$  and  $b = -0.42$  for the selected proton tracks. In this way, we are able to use  $dE/dx$ , reconstructed independently from charge deposit, and compare to models of energy loss by ionization.

## 4.2 Event selection

In this study we use protons emerging from neutrino interactions in argon. We choose a well selected sample of events with one muon and two protons ( $\nu_\mu$  charged current two protons (we refer to the sample as  $1\mu 2p$ )) because of the low contamination of other particle species within the selected protons and the very well reconstructed vertex of the interaction. Events with a muon plus two protons are produced almost exclusively by neutrino interactions, and not cosmic ray events, as verified using off-beam data. Having three tracks sharing the same vertex allows for better reconstruction resolution. For the purpose of this study we are interested in this sample due to its high purity of selected proton candidates.

The event selection is based on a set of cuts designed to select  $\nu_\mu$  with  $1\mu 2p$  interactions in the TPC fiducial volume. We take advantage of the very specific number of charged particles and the absence of  $e^\pm/\pi^0$  in our signal definition which leaves us with a well defined number of reconstructed tracks.

For the  $1\mu 2p$  events, the signature is three tracks originating from the same vertex, one each consistent with a muon and two protons. The cuts we apply in the selection are as follows:

- **Beam window:** 32 photomultiplier tubes are used in MicroBooNE to identify scintillation light information from particles travelling inside the TPC. In order to select neutrino interactions, we require there to be a photomultiplier photon detected signal coincident with the beam spill.
- **Vertex:** The reconstructed neutrino vertex is required to be in the fiducial volume. The fiducial volume (FV) is defined as the region in the TPC for which  $x_{\min} + 10 \text{ cm} < x < x_{\max} - 10 \text{ cm}$ ,  $y_{\min} + 20 \text{ cm} < y < y_{\max} - 20 \text{ cm}$  and  $z_{\min} + 10 \text{ cm} < z < z_{\max} - 10 \text{ cm}$ , where  $x_{\min} = 0 \text{ cm}$ ,  $x_{\max} = 256.35 \text{ cm}$ ,  $y_{\min} = -116.5 \text{ cm}$ ,  $y_{\max} = 116.5 \text{ cm}$ ,  $z_{\min} = 0 \text{ cm}$  and  $z_{\max} = 1036.8 \text{ cm}$  are the boundaries of the TPC.
- **Three tracks cut:** Only three tracks are associated to the vertex within a 5 cm radius. If more than one candidate is present in an event, the one where the sum of the distance between the start position of each track to each other is smallest is selected. This avoids cosmic events misreconstructed as coming from a neutrino interaction.
- **Proton containment:** The leading particle, defined as the longest track, is taken as the muon candidate; the remaining two tracks are our proton candidates. These two protons are required to be contained in the TPC FV to aid in particle identification.

- **Minimum number of hits:** For each track we require a minimum number of 10 hits in total, summing all three planes. In order to have the most reliable calorimetry information, we also require at least 5 hits in the collection plane. This is applied to each track.
- **Particle identification (PID) cut:** We use the  $\chi^2$  test with respect to a proton hypothesis in the  $dE/dx$  versus residual range curves, from Bethe-Bloch predictions, to discriminate MIP (minimum ionization particle) with respect to non-MIP particles. Within the Geant4 simulation, the residual range is sampled with a bin size of 0.08 cm.

For each selected track (either in MC or data) we obtain the reconstructed  $dE/dx$  per hit and calculate the  $\chi^2$  between the reconstructed and the Geant4-determined mean  $dE/dx$  at each given residual range bin. These  $\chi^2$  values are then summed for all hits on the selected track.

To avoid mis-estimation of the track range, we exclude the first and last hits of the track from this calculation. This is due to the fact that the residual range calculation for the first and last hit may be wrong since the exact position of the hit between the wires is unknown. It also avoids complications from particle activity effects (to avoid hits from soft protons that don't make tracks) and energy deposition overlap at the interaction vertex.

The  $\chi^2$  value is then normalized by the number of degrees of freedom (d.o.f.), which correspond to the number of hits in the collection plane. The  $\chi^2$  value can be determined for several particle assumptions, but in this analysis we exclusively use the proton hypothesis (thus the *proton* subscript).

$$PID = \chi_{proton}^2 / d.o.f. = \sum_{hit} \left( \frac{(dE/dx_{measured} - dE/dx_{theory})}{\sigma_{dE/dx}} \right)^2 / d.o.f., \quad (4.4)$$

where  $\sigma_{dE/dx}$  is the estimated resolution in measuring a fixed  $dE/dx$ , the subscript *measured* and *theory* corresponds to the  $dE/dx$  measured at the wires using the charge deposit information and the predicted by Geant4 respectively. Values used for error resolution in  $dE/dx$  are taken from studies performed by the ArgoNeuT Collaboration. This does not take into account the 3 mm wire spacing in MicroBooNE (compared to the 4 mm wire spacing in ArgoNeuT), which should lead to overestimated error in resolution.

Taking into account both the particle discrimination (muon *versus* proton) and the data/MC shape agreement, we apply a PID (particle identification) requirement that identifies protons as the tracks with low  $\chi_{proton}^2 / d.o.f.$  and muons as tracks with high  $\chi_{proton}^2 / d.o.f.$

An iterative approach is required when studying recombination effects. To perform such studies it is necessary to cover a broad spectrum of charge deposit per hit. This requires the use of highly ionizing particles, which must be selected. In a LArTPC, ionization charge is used for particle identification. Thus, an initial guess of recombination corrections need to be applied, for which we employ the modified box model with the parameters measured by ArgoNeuT. By using this method for PID, we are confident we select protons since the method relies mainly on the shape of the reconstructed  $dE/dx$  rather than averaged values per track. In this way, the distinction between a proton and a muon is much clearer.

Once the recombination correction is applied, we can perform particle identification using less information (as for example, a smaller number of hits) and particle discrimination that requires better calorimetry resolution, like kaon identification.

- **Shower veto:** We remove events with a shower reconstructed within 15 cm of the vertex, both to reduce  $\pi^0$  contamination and to reduce background caused by tracks misreconstructed as showers.

The purity of the selected protons is above 90%, based on MC simulation. A total of 226 protons candidates are selected in the neutrino beam data for this analysis.

With this proton sample we study two different recombination models: the modified box model, eq. 4.1, and Birks' law, eq. 4.2.

### 4.3 Analysis method

The comparison of these two models with the MicroBooNE proton dataset (described in sec. 4.2) is shown in figure 21. In this figure, the measured  $dQ/dx$ , after calibration, is shown with respect to the theoretically predicted energy deposit  $dE/dx_{\text{range}}$ , computed from the proton range (eq.4.3).

Figure 21 shows the comparison of our selected proton data with the modified box and Birks' law model (left), and compared to the MC using the same approach for the proton selection and the  $dE/dx$  estimation (right). The red curve corresponds to Birks' law and the black curve corresponds to the modified box model, using the parameters described.

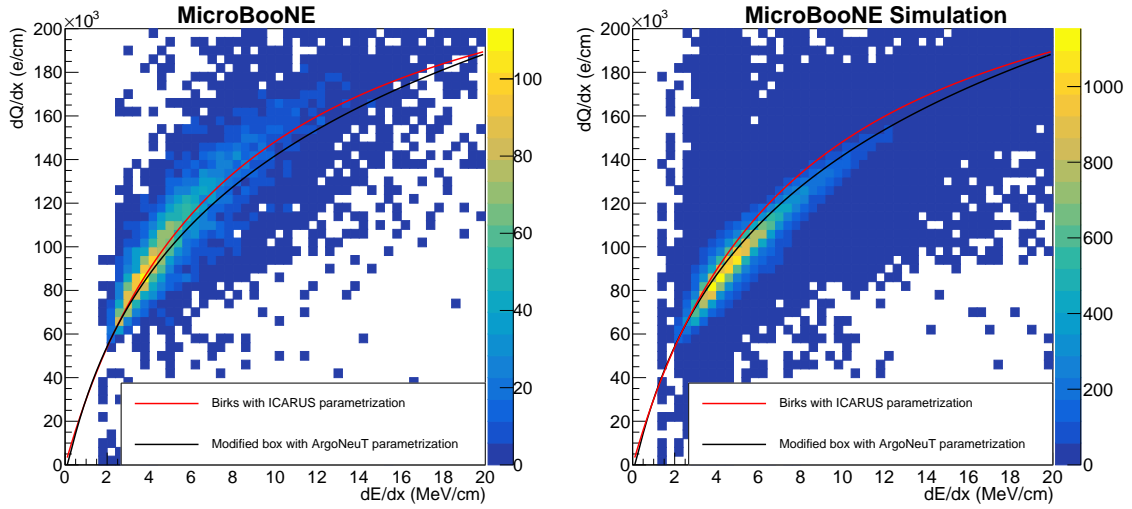


**Figure 21.** Left: proton selected tracks in data comparing the measured  $dQ/dx$  vs.  $dE/dx_{\text{range}}$  assuming all selected tracks are protons. Right: same comparison approach using MC selected protons. The red curve corresponds to Birks' law and black curve to the modified box model, using the parameters described in this paper.

We can observe from figure 21 (left) that there is good agreement of data with Birks' law and the modified box model at low  $dE/dx$ , as expected. Low  $dE/dx$  corresponds to the minimum ionizing particle region, which has been calibrated with muons previously. At higher  $dE/dx$ , the

data shows a lower recombination effect than the one predicted by the two models with the current parametrization. As expected, the MC agrees better with the parametrized models for the modified box model, black curve, since it is the one used for the simulation.

Due to the correlation between the electric field and the parameters from both the modified model and Birks' law, it is difficult to establish if our discrepancy is due to the parametrization of the models or the electric field estimation. Due to the high number of cosmic ray events producing space charge effects and thus electric field distortions, we expect that our electric field is non-uniform. For this reason, further studies within MicroBooNE will apply an electric field map that will allow decoupling these effects. For the current calibration of the MicroBooNE detector, we adopt an effective approach that takes into account that  $\beta'$  (in the modified box model) and  $k$  (in Birks' law) are functions of the electric field. As well, the electric field distortions affect the  $dQ/dx$  calibration, so that  $\alpha$  (modified box model), and  $A$  (Birks' law) should be correlated with the electric field. It is either possible that the recombination model parameters derived at other experiments are not correct at our electric field, or that the electric field distortions may be part of the problem but not necessarily the full problem. Knowing this, we proceed by applying *effective recombination* parameters, which in this case will take into account both the recombination corrections and the electric field distortions rather than producing a recombination measurement.

We obtain the *effective recombination* parameters by applying a fit of our selected proton data to the MC. We produce a  $\chi^2$  fit to the  $dQ/dx$  mean value per each  $dE/dx$  bin in data to the MC, and obtain the parameters ( $\alpha$  and  $\beta'$  for the modified box model, and  $A_B$  and  $k$  for Birks' law) that minimizes this  $\chi^2$ . From the data,  $dQ/dx$  in ( $e/cm$ ) comes from the conversion obtained in table 1, and the  $dE/dx$  is the  $dE/dx_{range}$  using the residual ranges, as described before. From the MC,  $dE/dx$  is also obtained using residual range information,  $dE/dx_{range}$ , and the  $dQ/dx$  is converted from  $dE/dx_{range}$  using the recombination model (modified box or Birks' law). The  $\chi^2$  is given by:

$$\chi^2 = \sum_{dE/dx_{range}^{DATA}} \left( \frac{dQ/dx(\alpha, \beta', dE/dx_{range}^{MC}) - dQ/dx_{measured}^{DATA}}{\sqrt{\left(\sigma_{dE/dx_{range}^{DATA}}^2 + \sigma_{dE/dx_{range}^{MC}}^2\right)}} \right)^2. \quad (4.5)$$

The obtained values from the two fits performed, one using the box model and the other using Birks' law are in table 2, including the uncertainties from the fit coming from statistics and the systematic variation to the data curve. To obtain these result, we assume an electric field of 0.273 kV/cm, which is the nominal electric field in MicroBooNE.

The effect of the obtained results can be clearly observed in figure 22, which shows the same distributions as figure 21 but now including the model curves (from modified box model, left, and Birks' law, right) using the newly obtained parameters, compared to the selected proton data. The black curve represents the modified box model with the original parameters and the blue curve uses the new parameters. The red curve is the Birks' law with the original parameters and the green curve uses the new parameters.

**Table 2.** *Effective recombination* parameters obtained from the fit of MicroBooNE proton data to the model. Uncertainties comes from statistics and systematic variation to the data curve.

	values from ref. [12] [24]	new value
modified box model $\alpha$	$(0.93 \pm 0.02)$	$(0.92 \pm 0.02)$
modified box model $\beta'$ (kV/cm)(g/cm <sup>2</sup> )/MeV	$(0.212 \pm 0.002)$	$(0.184 \pm 0.002)$
Birks' law $A_B$	$(0.800 \pm 0.003)$	$(0.816 \pm 0.012)$
Birks' law $k$ (kV/cm)(g/cm <sup>2</sup> )/MeV	$(0.0486 \pm 0.0006)$	$(0.045 \pm 0.001)$

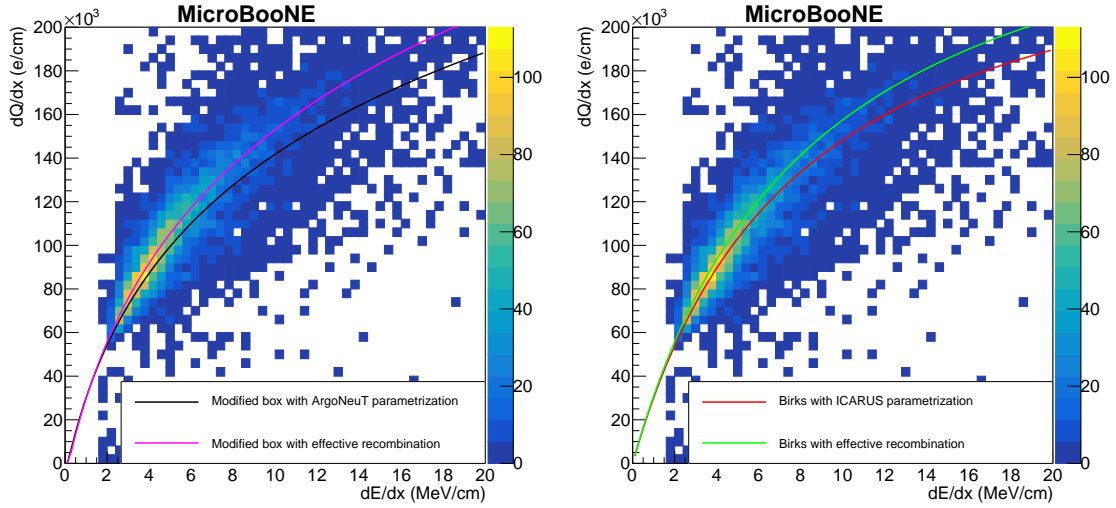


**Figure 22.** Proton selected tracks in data comparing the measured  $dQ/dx$  vs.  $dE/dx_{\text{range}}$  assuming all selected tracks are protons. Left: the black curve represents the modified box model with the original parameters and the blue curve uses the new parameters from table 2. Right: the red curve is the Birks' law with the original parameters and the green curve uses the new parameters from table 2.

#### 4.3.1 Validation after applying new parameters

We apply the obtained results from the *effective recombination* to compute  $dE/dx$  using the calibrated  $dQ/dx$ . The newly obtained  $dE/dx$  are compared to the Bethe-Bloch prediction with respect to residual range in figure 23. The distribution corresponds to the MicroBooNE neutrino data. Good agreement between the selected candidates and the central Bethe-Bloch prediction for protons can be seen.

## 4.4 Results

We have applied an *effective recombination* parametrization using the modified box model, convoluting non-uniformities in the electric field and the recombination parameters. An updated electric

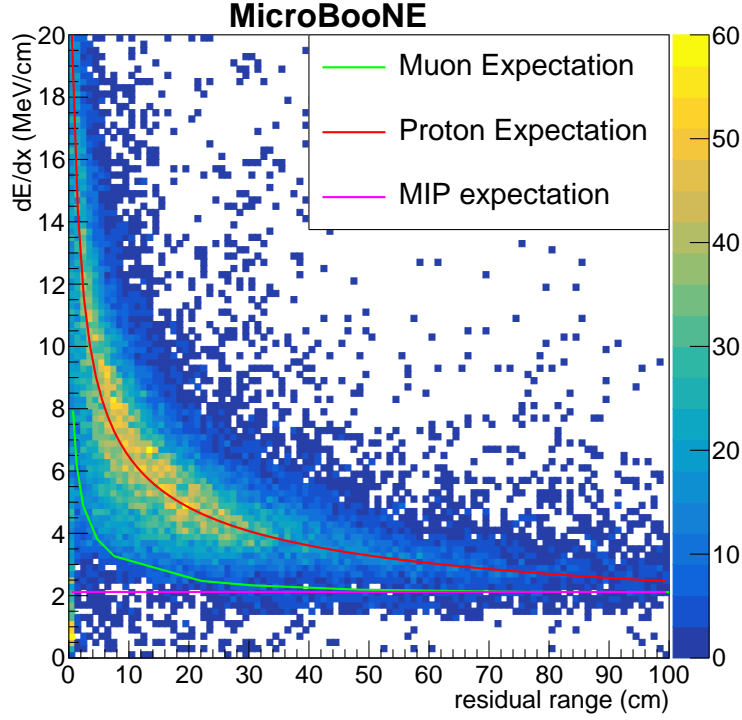


**Figure 23.**  $dE/dx$  vs residual range for contained tracks within the selected  $\nu_\mu$  CC inclusive sample, with a proton PID requirement, for on-beam data. *Effective recombination* has been applied to compute  $dE/dx$  values. Theoretical prediction of the Bethe-Bloch equation for the different particle types are included.

field mapping, measured using both cosmic and laser data in the MicroBooNE detector, will allow us in future to estimate the effect off a non-uniform electric field on the extraction of recombination parameters at MicroBooNE.

For this publication, we show that by using muon tracks we are able to calibrate the detector for the angular and electronics response over time. We show that by using selected neutrino-induced protons we are able to correct for both electric field and recombination effects with enough accuracy to perform particle identification.

Table 3 shows the purity and efficiency of the selected muons and protons, estimated from the MC sample. Purity is defined as the quantity of particles from an specific specie which has been correctly identified the particle type, divided by the total number of particles of that specie in the sample.

The result of the calibration procedure presented here is showed in figure 24. The distributions on the left show the  $dE/dx$  per deposited hit of the selected protons in data compared to those from the simulation. We observe a distribution reasonably well described by the simulation, for the main purpose of particle identification over most of the energy deposit range. We still have wider  $dE/dx$  in data than MC, this is due to the different smearing in data than MC for the energy deposit. In this analysis the correction applied mostly affects the central values. The efforts within the MicroBooNE collaboration to better understand the signal deposited in the readout wires and

**Table 3.** Purities for selected muons and protons in the MC, after applying the PID method and the calibration with the recombination corrections. Third column shows the efficiency of selecting the corresponding particle with respect the total number of particles of this specie before applying the PID cut.

particle type	purity	efficiency
selected muons	94%	99%
selected protons	93%	85%

distortion effects, as the ones producing spatial and electric field distortions, are being implemented in the new detector simulation and will improve residual discrepancies. We also show the  $dE/dx$  per deposited hit for selected protons and muons from data, right. We can clearly see from the figure that protons and muons can be well identified and have different widths in  $dE/dx$  as expected, due to the higher ionizing nature of the protons with respect to muons.

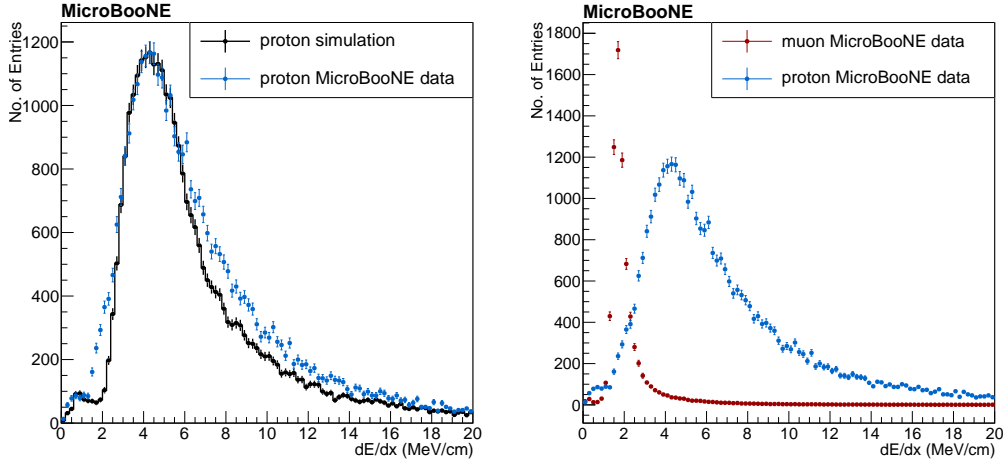


**Figure 24.** Left:  $dE/dx$  per hit for tracks selected as a proton candidate from MicroBooNE data compared to simulated protons. Right:  $dE/dx$  per hit for tracks selected as muons compared to the ones selected as protons in data, right.

## 5 Conclusions

In this paper, we describe for the first time a method that calibrates a LArTPC using muons and protons. We use crossing muons to remove spatial and temporal variations in the detector response. We use stopping muons to determine the absolute energy scale for minimum ionizing particles. We use stopping protons to calibrate the relation between measured charge and energy loss for highly ionizing particles. The most probable value of calibrated energy loss agrees with expectation. The calibrated energy loss per unit length is used in particle identification and energy reconstruction. This method can be followed by other LArTPC experiments to calibrate their detectors.

## Acknowledgements

This document was prepared by the MicroBooNE collaboration using the resources of the Fermi National Accelerator Laboratory (Fermilab), a U.S. Department of Energy, Office of Science, HEP User Facility. Fermilab is managed by Fermi Research Alliance, LLC (FRA), acting under Contract No. DE-AC02-07CH11359. MicroBooNE is supported by the following: the U.S. Department of Energy, Office of Science, Offices of High Energy Physics and Nuclear Physics; the U.S. National Science Foundation; the Swiss National Science Foundation; the Science and Technology Facilities Council (STFC), part of the United Kingdom Research and Innovation; and The Royal Society (United Kingdom). Additional support for the laser calibration system and cosmic ray tagger was provided by the Albert Einstein Center for Fundamental Physics, Bern, Switzerland.

## References

- [1] R. Acciarri *et al.* (MicroBooNE Collaboration), “Design and construction of the MicroBooNE detector”, JINST 12 (2017), P02017 [arXiv:1612.05824].
- [2] R. Acciarri *et al.* (MicroBooNE Collaboration), “Ionization Electron Signal Processing in Single Phase LAr TPCs I: Algorithm Description and Quantitative Evaluation with MicroBooNE Simulation”, JINST 13 (2018), P07006 [arXiv:1802.08709].
- [3] R. Acciarri *et al.* (MicroBooNE Collaboration), “Ionization Electron Signal Processing in Single Phase LAr TPCs II: Data/Simulation Comparison and Performance in MicroBooNE”, JINST 13 (2018), P07007 [arXiv:1804.02583].
- [4] R. Acciarri *et al.* (MicroBooNE Collaboration), “Noise Characterization and Filtering in the MicroBooNE Liquid Argon TPC”, JINST 12 (2017) P08003 [arXiv:1705.07341].
- [5] M. Mooney, “The MicroBooNE Experiment and the impact of Space Charge Effects”, Proceeding of DPF 2015 Meeting of APS, [arXiv:1511.01563].
- [6] E. Buckley *et al.*, “A study of ionization electrons drifting over large distances in liquid argon”, Nucl. Instrum. and Methods in Physics Research A 275, 364-372 (1989).
- [7] A. Bettini *et al.*, “A study of the factors affecting the electron lifetime in ultra-pure liquid argon”, Nucl. Instrum. and Methods in Physics Research A 305, 177-186 (1991).
- [8] S. Amoruso *et al.* (ICARUS Collaboration), “Analysis of the liquid argon purity in the ICARUS T600 TPC”, Nucl. Instrum. and Methods in Physics Research A 516, 68-79 (2014).
- [9] C. Bromberg *et al.* (LongBo Collaboration), “Design and operation of LongBo: a 2 m long drift liquid argon TPC”, JINST 10 (2015) P07015.
- [10] C. Anderson *et al.* (ArgoNeuT Collaboration), “The ArgoNeut detector in the Numi low-energy beam at Fermilab”, JINST 7 (2012) P10019.
- [11] Y. Li *et al.*, Measurement of Longitudinal Electron Diffusion in Liquid Argon, arXiv:1508.07059, Nucl. Instrum. Meth. A816 P160-170 (2016)
- [12] R. Acciarri *et al.* (ArgoNeuT Collaboration), “A study of electron recombination using highly ionizing particles in the ArgoNeuT Liquid Argon TPC”, JINST 8 (2013) P08005.
- [13] S. Amoruso *et al.* (ICARUS Collaboration), “Study of electron recombination in liquid argon with the ICARUS TPC”, Nucl. Instrum. Meth. A523 P275-286 (2004)



- [14] J. J. Hartnell, “Measurement of the Calorimetric Energy Scale in MINOS,” FERMILAB-THESIS-2005-51, doi:10.2172/875528.
- [15] G. D. Germonimo, et al., “Front-End ASIC for a Liquid Argon TPC”, IEEE Trans. Nucl. Sci 58 (2011) 1376-85.
- [16] D. Heck, G. Schatz, T. Thouw, J. Knapp and J. N. Capdevielle, FZKA-6019.
- [17] C. Andreopoulos *et al.*, Nucl. Instrum. Meth. A **614**, 87 (2010).
- [18] R. Acciarri *et al.* (MicroBooNE Collaboration), “The Pandora Multi-Algorithm Approach to Automated Pattern Recognition of Cosmic Ray Muon and Neutrino Events in the MicroBooNE Detector”, arXiv:1708.03135, Eur. Phys. J. C78, 1, 82 (2018).
- [19] R. Acciarri *et al.* (MicroBooNE Collaboration), “First Measurement of Muon Neutrino Charged Current Neutral Pion Production on Argon with the MicroBooNE LAr TPC”, Phys. Rev. D99 (2019) 091102(R) [arXiv:1811.02700].
- [20] Convoluted Landau and Gaussian Fitting Function,  
<https://root.cern.ch/root/html/tutorials/fit/langaus.C.html>
- [21] Donald E. Groom, Nikolai V. Mokhov, Sergei I. Striganov, Muon Stopping Power and Range Tables 10 MeV - 100 TeV, Atomic Data and Nuclear Data Tables, Vol. 76, No. 2, July 2001.
- [22] Passage of particle through matter,  
<http://pdg.ge.infn.it/2014/reviews/rpp2014-rev-passage-particles-matter.pdf>
- [23] J. Thomas and D. A. Imel, “Recombination of electron-ion pairs in liquid argon and liquid xenon”, Phys. Rev. A36, 614-616 (1987).
- [24] John B. Birks, “The Theory and practice of scintillation counting”, Pergamon Press (1964).